



Vehicle System Dynamics: International Journal of Vehicle Mechanics and Mobility

Publication details, including instructions for authors and
subscription information:

<http://www.tandfonline.com/loi/nvsvd20>

A 3D Brush-type Dynamic Tire Friction Model

Joško Deur^a, Jahan Asgari & Davor Hrovat

^a Faculty of Mechanical Engineering and Naval
Architecture University of Zagreb I. Lučića 5

Version of record first published: 09 Aug 2010.

To cite this article: Joško Deur, Jahan Asgari & Davor Hrovat (2004): A 3D Brush-type Dynamic Tire Friction Model, *Vehicle System Dynamics: International Journal of Vehicle Mechanics and Mobility*, 42:3, 133-173

To link to this article: <http://dx.doi.org/10.1080/00423110412331282887>

PLEASE SCROLL DOWN FOR ARTICLE

Full terms and conditions of use: <http://www.tandfonline.com/page/terms-and-conditions>

This article may be used for research, teaching, and private study purposes. Any substantial or systematic reproduction, redistribution, reselling, loan, sub-licensing, systematic supply, or distribution in any form to anyone is expressly forbidden.

The publisher does not give any warranty express or implied or make any representation that the contents will be complete or accurate or up to date. The accuracy of any instructions, formulae, and drug doses should be independently verified with primary sources. The publisher shall not be liable for any loss, actions, claims, proceedings, demand, or costs or damages whatsoever or howsoever caused arising directly or indirectly in connection with or arising out of the use of this material.

A 3D Brush-type Dynamic Tire Friction Model

JOŠKO DEUR¹, JAHAN ASGARI² AND DAVOR HROVAT²

SUMMARY

The use of advanced dynamic friction models can improve the brush-type tire friction models. This paper presents a 3D dynamic brush model based on the LuGre friction model. The model describes the dynamics of longitudinal and lateral tire friction forces, as well as the self aligning torque dynamics. It has been originally derived in a distributed-parameter form, and then transformed to a simpler lumped-parameter form with only three internal states. Both uniform and non-uniform normal pressure distributions are considered. The model has analytical solution for steady-state conditions. The steady-state behavior is validated with respect to “magic” formula static model, which served as an “ideal” benchmark. The lumped model dynamic behavior is validated by comparing its time-responses with original distributed model responses. The model parameterization with respect to normal force and other tire/road parameters is considered as well.

1. INTRODUCTION

Vehicle motion is primarily determined by the friction forces transferred to the road by the tires. Therefore, a proper tire friction model is one of the key elements of a complete vehicle model intended for the use in different vehicle dynamics simulation studies for handling applications. In addition, the tire friction model represents a basis for the development of tire-road friction estimators and various vehicle dynamics control systems (including ABS and traction control systems).

Tire friction is traditionally modeled by utilizing a static model, which can be described by brush model expressions [1–4] or empirical formulae (e.g., “magic” formula [4–6]). However, there has been a significant research interest in modeling the tire friction dynamics in recent years. This interest has been motivated by two observations: (i) the tire friction dynamics (caused by the tire tread compliance) may

¹Faculty of Mechanical Engineering and Naval Architecture, University of Zagreb, I. Lučića 5, HR-10000, Zagreb, Croatia.

²Ford Research and Advanced Engineering, MD 2036, P.O. Box 2053, Dearborn, MI 48121-2053, USA.

³Address correspondence to: Joško Deur, Faculty of Mechanical Engineering and Naval Architecture, University of Zagreb, I. Lučića 5, HR-10000, Zagreb, Croatia; Tel.: +385-1-6168-372; Fax: +385-1-6168-351; E-mail: josko.deur@fsb.hr

be important from the standpoint of development of high-performance vehicle dynamics systems [7–9], and (ii) numerical difficulties of the traditional static tire models at low vehicle speeds can be avoided by using a dynamic tire model [9, 10].

The tire friction dynamics can conveniently be included into the traditional brush model, as proposed in [7, 8]. This model captures all important aspects of the tire friction dynamics. However, the model has a complex distributed-parameter form, with a large number of internal (bristle deflection) states. This affects the model computing efficiency, and makes the model inconvenient for the purpose of controller/estimator design. A more pragmatic tire friction modeling approach has led to the relaxation length-based model [9–13]. The model represents an extension of the “magic” formula-based static model with a simple lumped-parameter brush sub-model of tire tread compliance. Thus, it can be regarded as a semi-empirical quasi-static lumped model. The overall 3D tire friction model from [9, 11] describes the longitudinal/lateral force and self aligning torque dynamics, and has three internal states.

The brush model from [7, 8] includes a traditional dynamic friction description (cf. [14]), which consists of the linear presliding displacement curve for the stick (adhesion) region and a generalized Stribeck speed-dependent curve for the slip (sliding) region. It has been recognized in [15] that the use of more advanced dynamic friction models could enhance the tire friction model. The second-order dynamic friction model from [16] is used in [15], in order to accurately describe the nonlinear presliding displacement curve, and to achieve a continuous transition from stick to slip region. This results in a compact distributed model for longitudinal motion, which has an accurate analytical solution for the tire static curve (mu-slip curve).

Another longitudinal brush model, based on the first-order LuGre dynamic friction model [17], has been proposed in [18]. Its advantages compared to the model from [15] are more accurate description of different friction dynamic effects, simpler first-order form, and physical meaning of parameters. The model has an analytical solution for the mu-slip curve, and it can be transformed to a single-state (lumped) form. However, the static curve and the lumped model derived in [18] had inconsistent forms, as shown in [19, 20]. The static curve was very sensitive to the wheel/vehicle speed, as a consequence of improper definition of tire force damping term. The lumped model missed the important tire-specific convective term, which resulted in incorrect sliding bearing-like mu-slip curve. This is particularly critical in the low-slip region where most of vehicle operations occur.

The longitudinal LuGre tire friction model from [18] has been modified and extended in [19, 20], in order to provide correct prediction of tire static and dynamic behavior. The model has then been further extended and validated for the case of combined longitudinal and lateral motion [21, 22]. A non-uniform normal pressure distribution is introduced in [21, 22] with the aim to obtain consistent self aligning torque behavior. A three-state 3D lumped dynamic model for the non-uniform normal pressure distribution has been derived in [23]. Some empirical extensions,

parameterization, and validation of the model have been considered in the subsequent internal reports [24–27] (see also [28]).

The recent paper [29] has revised the original model from [18] (for the pure longitudinal motion only), but, unfortunately, without adequate referring to [19–23] where the main revisions and extension were first developed and published (see [30]). Also, an extension of the original model for combined longitudinal and lateral motion has been proposed in [31]. However, that model does not adequately describe the friction coupling in longitudinal and lateral directions, and does not consider the important case of non-uniform normal pressure distribution.

This paper presents the overall 3D LuGre dynamic tire friction model based on [19–27]. Section 2 defines the problem of tire friction modeling and describes the brush representation of tire-road friction contact. Different dynamic friction models for the bristle-to-road contact are presented in Section 3. The distributed LuGre dynamic (and static) tire friction model is derived in Section 4. It is transformed to the lumped form in Section 5. The model is validated in Section 6. Section 7 presents some mostly-empirical model extensions which are aimed to increase the accuracy of the model static curves. Model parameterization with respect to normal force and other tire-road conditions are considered in Section 8. Concluding remarks are given in Section 9.

2. BRUSH REPRESENTATION OF TIRE MODEL

The tire coordinate system is defined in Figure 1 [3, 32]. The tire model input quantities are: normal force F_z , wheel hub translational speed v , wheel hub rotational speed ω ,

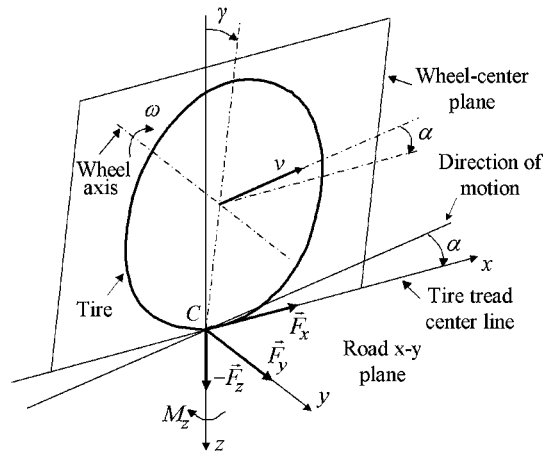


Fig. 1. Coordinate system of tire.

Downloaded by [University of Arizona] at 12:24 19 December 2012

Downloaded by [University of Arizona] at 12:24 19 December 2012

Downloaded by [University of Arizona] at 12:24 19 December 2012

Downloaded by [University of Arizona] at 12:24 19 December 2012

Downloaded by [University of Arizona] at 12:24 19 December 2012

Downloaded by [University of Arizona] at 12:24 19 December 2012

Downloaded by [University of Arizona] at 12:24 19 December 2012



Downloaded by [University of Arizona] at 12:24 19 December 2012

aligning torque static curves is taken into account by making the bristle stiffness lower in lateral than longitudinal direction [1; 3, p. 145] (Sections 4 and 8). In order to capture the dynamic modes caused by the torsional, longitudinal, and lateral sidewall compliance, the tire friction model needs to be extended by the multi-body tire dynamics, as done in [4, 8, 9, 13].

The longitudinal, lateral, and absolute values of the relative speed between a bristle base point and the corresponding tip in the adhesion region are given by the following relations, respectively [1–3] (Fig. 2):

$$v_{rx} = r\omega - v \cos \alpha, \quad (2)$$

$$v_{ry} = v \sin \alpha, \quad (3)$$

$$v_r = \sqrt{v_{rx}^2 + v_{ry}^2}. \quad (4)$$

The case $v_{rx} \geq 0$ corresponds to driving (traction), while braking is determined by $v_{rx} < 0$ (cf. Eq. (1)). It should be noted that, in reality, the relative speeds v_{rx} , v_{ry} , and v_r vary along the contact length due to turning, camber, and lateral sidewall compliance effects, namely that Equations (2)–(4) should be extended with longitudinal bristle position (ζ)-dependent terms [3, 4, 8, 32]. However, these effects are usually neglected, in order to obtain a simple (analytical) tire model.

Friction transferred from a base point to the road may conveniently be described for pure longitudinal motion ($\alpha = 0$) by an equivalent mechanical model shown in Figure 3a [33]. The model consists of a mass-less spring with the stiffness coefficient σ_0 , which accounts for the bristle compliance effect, and a mass-less tip/road friction element with

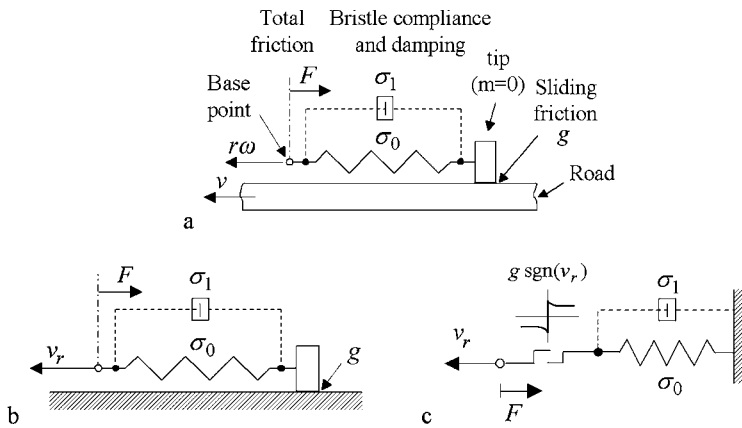


Fig. 3. Equivalent model of bristle friction for pure longitudinal motion ($\alpha = 0$) in wheel coordinate system (a), and road coordinate systems (b) or equivalently as shown in (c).

a static friction characteristic g . Figure 3b shows the equivalent model given in the road (ground) coordinate system. The model shown in Figure 3b may be regarded as a dynamic friction model, with an internal state which corresponds to the spring deflection (bristle horizontal deflection), as also shown in Figure 3c based on [19].

Linear tire/road contact line shown in Figure 2 corresponds to the case of full tire/road adhesion and constant slip quantities s and α (i.e., for the full-adhesion steady-state operation). Outside the low-slip region, tips of some bristles will slide over the road. In such a sliding regime, the tip moves with respect to wheel axis with the same speed $r\omega$ as the base point (under the steady-state conditions), while the initial *tip/road contact point* (at $\zeta = 0$) continues to move with the wheel center speed v . The tip transfers the sliding friction $g(v_r)$ to the road. The bristle deflection becomes constant (for the uniform normal pressure distribution), and the tip path becomes parallel to the x -axis (dashed contact line in Fig. 2). The slip speed equations (2)–(4) are valid for the sliding region as well, assuming that they represent the relative speeds between the bristle base point and the corresponding tip/road contact point. The described slip-region behavior can clearly be explained by the internal structure of the friction model shown in Figure 3.

3. MODELING OF BRISTLE FRICTION

The traditional way of describing the bristle friction equivalent model given in Figure 3b and c is to separately describe the friction behavior for the adhesion (stick) region and the sliding region [1–3, 7]. The bristle deflection process in the adhesion region is usually described by the linear stress-strain curve. It is anticipated that the use of more comprehensive dynamic friction models, such as those proposed in [16, 17, 34, 35], can result in more accurate tire friction models.

3.1. Friction Effects

Friction is usually described by the static friction curve shown in Figure 4a. This curve includes the following static friction effects: Coulomb or dry friction $F_C \operatorname{sgn}(v_r)$, viscous friction, Stribeck friction at low relative speeds, and stiction in the zero-speed region. The curve can be described as [17, 34, 35]

$$F(v_r) = [g(v_r) + \sigma_2 |v_r|] \operatorname{sgn}(v_r), \quad (5)$$

where $\sigma_2 |v_r|$ is the viscous friction term, and $g(v_r)$ is the positive sliding friction function given by

$$g(v_r) = F_C + (F_S - F_C) e^{-|v_r/v_s|^\delta} \quad (6)$$

with F_C – Coulomb friction force, F_S – maximum static friction force, v_s – Stribeck speed, and δ – Stribeck exponent (typically $\delta \in [0.5, 2]$).

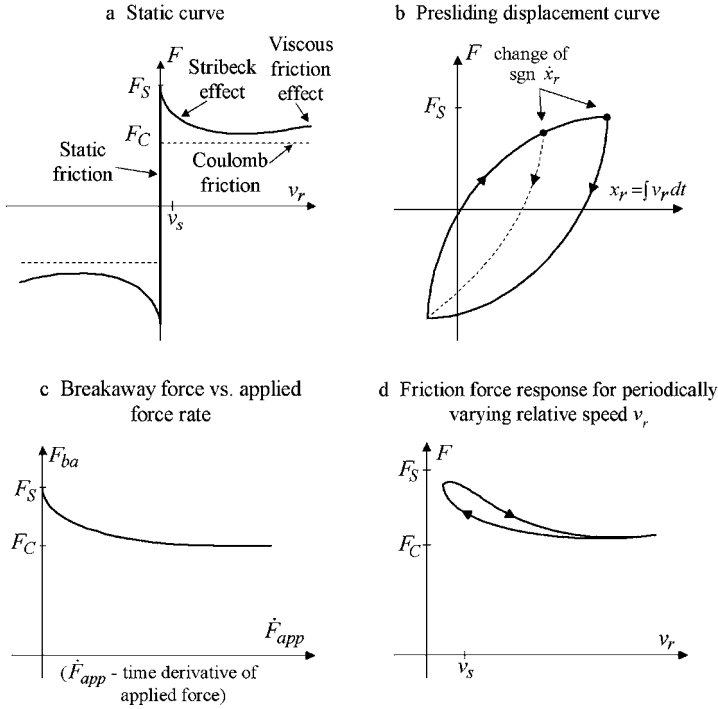


Fig. 4. Illustration of different static (a) and dynamic (b–d) friction effects.

The static friction model from Figure 4a cannot be implemented as a simulation model, because friction is not uniquely defined at zero speed. The problem may be overcome by using a finite-rate straight-line approximation of the stiction curve (so-called classical friction model) [14, 35], or by implementing separate friction “logic” for stick and slip regions [35–37]. However, physically more correct way of describing the stiction is to take into account the stiction dynamics described by the presliding displacement curve in Figure 4b. This curve corresponds to the hysteretic stress-strain curve which describes the process of elastic and plastic horizontal deformation of the bristle (or of the asperity contacts for a sliding or rolling bearing) [34, 38]. It implies that there is some varying relative displacement x_r (spring displacement in Fig. 3) between the contacting surfaces (in this case, between the base point and tip), before the real sliding occurs.

There are two other dynamic friction effects known from tribology experiments. According to the variable breakaway force effect (Fig. 4c), the breakaway force decreases from the maximum stiction F_S to the Coulomb friction force F_C as the rate of change of applied force (i.e., the rate of change of stiction) increases. This means

that the Stribeck effect (Fig. 4a) becomes less emphasized for more abrupt stick-to-slip transitions. According to the frictional lag effect (Fig. 4d), the low-speed friction response with respect to periodic change of relative speed closes a hysteretic loop around the static friction curve. The loop is wider for higher frequencies of relative speed.

3.2. Dynamic Friction Models

Dahl has described the hysteretic friction curve from Figures 4b and 5 by an exponential static relation $F(x_r, \text{sgn } \dot{x}_r)$ [38]. After transforming this relation into the time domain, the following first-order nonlinear dynamic friction model is obtained [38]:

$$\frac{dF}{dt} = \sigma_0 \left(v_r - \frac{F}{F_C} |v_r| \right). \quad (7)$$

The model can readily be transformed to the form $\tau(v_r)\dot{F} + F = F_C \text{sgn}(v_r)$, $\tau = F_C/(\sigma_0|v_r|)$ [39], which implies that the Dahl model can be regarded as the Coulomb model $F = F_C \text{sgn}(v_r)$ extended with the speed-dependent stiction lag during the change of motion direction.

The main weakness of the Dahl model is that it does not include the breakaway friction drop described by the Stribeck effect (Fig. 4a). This weakness is avoided in [7, 14, 34] by approximating the hysteretic presliding displacement curve in Figure 4a with a straight line (see Fig. 5), and saturating stiction to the speed dependent sliding

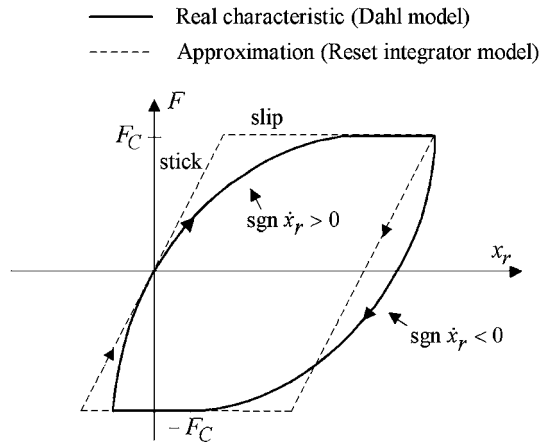


Fig. 5. Friction vs. displacement curve (for $F_S = F_C$).

friction force $g(v_r)$ given by Equation (6). This leads to the following dynamic friction model [7]:

$$\frac{dz}{dt} = v_r, \quad (8a)$$

$$F = \sigma_0 \text{sat} \left(z, \frac{g(v_r)}{\sigma_0} \right). \quad (8b)$$

Here, the friction state variable z corresponds to the horizontal bristle deflection (spring deflection in Fig. 3b and c), and sat is the saturation function (note that the correct saturation implementation assumes that z is saturated in the state Equation (8a) to avoid integrator windup). The model (8) is closely related to the reset integrator friction model proposed in [14]. The main difference is that (8) includes variable (speed-dependent) saturation level of the deflection variable z compared to the constant saturation level in [14]. The speed-dependent saturation level appears to be more realistic in terms of dynamic friction effects in Figure 4c and d. It should be mentioned that the output Equation (8b) should be extended with the damping term $\sigma_1 dz/dt$ [14], in order to capture the experimentally observed (weakly) damped stiction behavior. Note that the damping is naturally included in the Dahl model through the stiction hysteresis losses.

The main weaknesses of the friction model (8) are inaccurate presliding displacement curve (plastic deformation is neglected, i.e., linear bristle spring is assumed), and incompact mathematical form (a stick-slip switching logic is used). These weaknesses are avoided in an extension of the Dahl model with the Stribeck effect, as proposed in [17]. The constant Coulomb friction force F_C in the Dahl model (7) is simply replaced by the speed dependent sliding friction function $g(v_r)$. In addition, the linear stiction damping term and the linear viscous friction term (cf. Eq. (5)) are introduced. These modifications lead to the so-called LuGre¹ friction model² [17]:

$$\frac{dz}{dt} = v_r - \frac{\sigma_0 |v_r|}{g(v_r)} z, \quad (9a)$$

$$F = \sigma_0 z + \sigma_1 \frac{dz}{dt} + \sigma_2 v_r. \quad (9b)$$

It is shown in [17] that the LuGre model can capture not only the Stribeck and presliding displacement effects (Fig. 4a and b), but also the variable breakaway force

¹The model has been developed by the group of researchers from the Universities of **Lund** and **Grenoble**.

²It is interesting to note that the key Dahl model modification $F_C \rightarrow g(v_r)$, used in the LuGre friction model, was suggested (but apparently not realized) in [14, p. 355].

and frictional lag effects (Fig. 4c and d). Therefore, it is usually regarded as the most comprehensive control-oriented friction model to date.

3.3. Normal Force Dependence of Friction

It is well-known that the static friction curve in Figure 4a is approximately proportional to the normal force between the contacting surfaces (or to the tire normal force in the particular case) [34, 35]. However, it is not immediately clear how to include the normal force dependency in a dynamic friction model, such as the LuGre model (9). There are two ways of normal force realization [21, 22]: (i) scaling the sliding friction function g in the state Equation (9a) with the factor F_z/F_{z0} , where the model parameters correspond to the nominal normal force value F_{z0} ; and (ii) scaling the output Equation (9b) with the factor F_z/F_{z0} , which corresponds to the case of scaling both the function g and the stiffness coefficient σ_0 (assuming $\sigma_{1,2} \approx 0$).

It was hypothesized in [40] that the former (g -scaling) method of the variable normal force realization is more appropriate than the latter (f -scaling) method, but the latter has, nevertheless, been suggested for tire friction modeling [18]. In the tire modeling literature (e.g., [3]), the g -scaling method is commonly used, although it is known that the stiffness coefficient σ_0 (not only the function g) depends on the normal force F_z (see [1, 3, 19] and Section 8). It has been shown in [41], that the rolling bearing friction dynamics can accurately be modeled by using the f -scaling approach, namely that both σ_0 and g are proportional to the normal force F_z . The same approach has been generally proposed in [35, p. 1100]. It may be concluded, that it seems reasonable to include the normal force dependency in the friction model output equation (f -scaling), which in the case of LuGre model gives

$$F = \frac{F_z}{F_{z0}} \left(\sigma_0 z + \sigma_1 \frac{dz}{dt} + \sigma_2 v_r \right). \quad (10)$$

4. DISTRIBUTED TIRE FRICTION MODEL

Any of the dynamic friction models discussed in the previous section may be used to develop a brush tire friction model. The LuGre model is applied here, because of its apparent accuracy, and simple and compact mathematical form.

4.1. Distributed LuGre Model

According to the LuGre dynamic friction model (9), the bristle deflection process at the position ζ of the contact patch and at the time t can be described for pure

longitudinal motion ($\alpha = 0$; Fig. 3b and c) by the following first-order nonlinear differential equation [18]:

$$\frac{dz(\zeta, t)}{dt} = v_r(t) - \frac{\sigma_0 |v_r(t)|}{g(v_r(t))} z(\zeta, t). \quad (11)$$

The differential of the deflection variable z , as a function of two independent variables ζ and t , is given by

$$dz(\zeta, t) = \frac{\partial z(\zeta, t)}{\partial \zeta} d\zeta + \frac{\partial z(\zeta, t)}{\partial t} dt. \quad (12)$$

Rearranging Equation (12), and taking into account brush model relations (Fig. 2) yields [7, 19]:

$$\frac{\partial z(\zeta, t)}{\partial t} = \frac{dz(\zeta, t)}{dt} - \frac{\partial z(\zeta, t)}{\partial \zeta} \frac{d\zeta}{dt} = \frac{dz(\zeta, t)}{dt} - r|\omega| \frac{\partial z(\zeta, t)}{\partial \zeta}. \quad (13)$$

Inserting Equation (11) into Equation (13) yields the final partial differential equation of the LuGre tire friction model [18–20]

$$\frac{\partial z(\zeta, t)}{\partial t} = v_r - \frac{\sigma_0 |v_r|}{g(v_r)} z(\zeta, t) - r|\omega| \frac{\partial z(\zeta, t)}{\partial \zeta}. \quad (14)$$

In the case of combined longitudinal and lateral motion (Fig. 2), the bristles are deflected in both the longitudinal (x) and lateral (y) directions. Thus, Equation (14) is transferred into two equations for these two directions, which are represented by the vector equation

$$\frac{\partial z_{x,y}(\zeta, t)}{\partial t} = v_{rx,y} - \frac{\sigma_{0x,y} |v_{rx,y}|}{g_{x,y}(v_r, v_{rx,y})} z_{x,y}(\zeta, t) - r|\omega| \frac{\partial z_{x,y}(\zeta, t)}{\partial \zeta}, \quad (15)$$

where subscripts x, y point to the corresponding direction. Due to the anisotropic nature of tire [1, 3], different longitudinal and lateral stiffness coefficients σ_{0x} and σ_{0y} , respectively, are used in Equation (15). The longitudinal and lateral components $g_{x,y}$ of the tire/road sliding friction force $g(v_r)$ are positive according to the LuGre model structure [17, 19], and they are expressed as [1, 3]:

$$g_{x,y}(v_r, v_{rx,y}) = \left| \frac{v_{rx,y}}{v_r} \right| g(v_r). \quad (16)$$

Inserting Equation (16) into Equation (15) and rearranging yields the final deflection equations for combined longitudinal and lateral motion:

$$\frac{\partial z_{x,y}(\zeta, t)}{\partial t} = v_{rx,y} - \frac{\sigma_{0x,y} |v_r|}{g(v_r)} z_{x,y}(\zeta, t) - r|\omega| \frac{\partial z_{x,y}(\zeta, t)}{\partial \zeta}. \quad (17)$$

According to the output equation of the LuGre friction model (10), the longitudinal and lateral components of tire force contribution of a bristle at the position ζ in the tire central plane (defined per unit area of the contact patch) can be expressed as [19–23]

$$\varphi_{x,y}(\zeta, t) = \frac{\hat{p}(\zeta)}{LW} \left[\sigma_{0x,y} z_{x,y}(\zeta, t) + \sigma_{1(x,y)} \frac{\partial z_{x,y}(\zeta, t)}{\partial t} + \sigma_2 v_{rx,y} \right], \quad (18)$$

where $\hat{p}(\zeta)$ is the normalized (dimensionless) normal pressure distribution along the longitudinal axis x :

$$\hat{p}(\zeta) = \frac{p(\zeta)}{\bar{p}(\zeta)} = \frac{LW}{F_z} p(\zeta) \quad (19)$$

and L and W are length and width of the rectangular contact patch, respectively. The normal pressure distribution along the lateral axis y is assumed to be uniform.

The total longitudinal and lateral components of tire friction force are obtained by integrating the bristle force contributions over the contact patch area:

$$F_{x,y}(t) = \int_{-W/2}^{W/2} \int_0^L \varphi_{x,y}(\zeta, t) d\zeta dy = W \int_0^L \varphi_{x,y}(\zeta, t) d\zeta. \quad (20)$$

Accordingly, the self aligning torque is calculated as (Figs. 1 and 2, [2, 3]):

$$M_z(t) = W \int_0^L \varphi_y(t) \left(\frac{L}{2} - \zeta \right) d\zeta. \quad (21)$$

Note that Equations (20) and (21) correspond to the basic cases of zero horizontal and vertical shifts of tire static curves (ply steer, conicity, and rolling resistance are neglected), and zero residual torque. These (secondary) effects may be included in the model in the similar (empirical) way as done in [4–6]. Note also that Equation (21) neglects the torque contributions $-\varphi_x z_y$ and $\varphi_y z_x$ related to the shifts of the lines of action of the longitudinal and lateral force components, respectively [3, p. 148]. It has been confirmed by simulation that the influence of these torque contributions is very small due to $z_{x,y} \ll L/2$.

The distributed tire model, given by Equations (17)–(21), has an analytical solution for the steady-state case (see next subsection). However, in the general case of transient tire behavior, the model is discretized in space for a finite number of bristles, and solved numerically (finite difference approach, [7, 19]). The deflection state Equation (17) is discretized as

$$\dot{z}_{ix,y} = v_{rx,y} - \frac{\sigma_{0x,y} |v_r|}{g(v_r)} z_{ix,y} - r |\omega| \frac{N-1}{L} (z_{ix,y} - z_{(i-1)x,y}), \quad i = 2, \dots, N, \quad z_{1x,y} = 0, \quad (22)$$

where N is the total, sufficiently large number of bristles, and z_i is the horizontal deflection of the i^{th} bristle. In addition, summation instead of integration is used in

Equations (20) and (21). Note that the number of internal finite difference model states equals $2(N-1)$.

The distributed tire model contains two sub-models for the longitudinal (x) and lateral (y) axes of the tire coordinate system. These two sub-models have the same structure. They are coupled only in the sliding friction function $g(v_r)$ and the slip speed v_r itself (i.e., decoupled in the internal state variables $z_{x,y}$, cf. Eq. (17)). This coupling is missed in the LuGre tire friction model presented in [31]. It has been taken there that there are two independent friction functions $g_x(v_{rx})$ and $g_y(v_{ry})$ with two independent, quite different sets of parameters. In terms of brush model representation, this would mean that there are two bristles at any contact patch position, where one is deflected in x and the other in y direction. In reality, there is only a single bristle at any contact patch position, and, accordingly, a single (unique) friction force which is decomposed to its x and y components according to Equation (16). Applying the model from [31] can lead to missing the friction circle (or friction ellipse) as an essential tire property. Such a modeling concept has been viewed with some skepticism in [3, p. 155].

4.2. Static LuGre Model

For the steady-state operation, the term $\partial z_{x,y}(\zeta, t)/\partial t$ in Equation (17) equals zero. Thus, the partial differential Equation (17) is transformed to the ordinary differential equation in the space variable ζ , with the following solution [18–20]:³

$$z_{x,y}(\zeta) = \frac{v_{rx,y} g(v_r)}{|v_r| \sigma_{0x,y}} (1 - e^{-\zeta/Z_{x,y}}) \quad (23)$$

with the space constant $Z_{x,y}$ given by

$$Z_{x,y} = \left| \frac{r\omega}{v_r} \right| \frac{g(v_r)}{\sigma_{0x,y}}. \quad (24)$$

Inserting Equation (23) into Equation (18), and solving the integral Equations (20) and (21) for the case of **uniform normal pressure distribution** ($\hat{p}(\zeta) \equiv 1$) yields the following final expressions for the longitudinal and lateral steady-state tire forces F_x and F_y , and the self aligning torque M_z :

$$F_{x,y} = \frac{v_{rx,y}}{|v_r|} g(v_r) \left[1 - \frac{Z_{x,y}}{L} (1 - e^{-L/Z_{x,y}}) \right] + \sigma_2 v_{rx,y}, \quad (25a)$$

$$M_z = -\frac{v_{ry}}{|v_r|} g(v_r) Z_y \left[\frac{1}{2} - \frac{Z_y}{L} + \left(\frac{1}{2} + \frac{Z_y}{L} \right) e^{-L/Z_y} \right]. \quad (25b)$$

³ According to Equation (4), $v_r \geq 0$. Thus, $|v_r|$ in Equation (23) (and in the further equations for the tire static curves) can be replaced by v_r . The term $|v_r|$ is, though, used here in order to avoid the wrong conclusion that the scaling factor $v_{rx(y)}/|v_r|$ would be equal to 1 (instead of $\text{sgn}(v_r)$) in the case pure longitudinal (or pure lateral) motion, when $v_{rx(y)} = v_r$.

The static tire friction model (25) includes a singularity in the case of zero slip speed ($v_r = 0$, pure rolling).⁴ Observing that the tire forces and the self aligning torque are equal to zero in this case, the problem may be resolved by setting $F_{x,y} = 0$ and $M_z = 0$ if $|v_r| < \Delta_{vr}$, where Δ_{vr} is a small slip speed threshold. However, in some applications of the static model, it may be important to avoid the model discontinuity at the points $v_r = \pm \Delta_{vr}$. This can be done by using the Taylor series expansion of the model (25) around the zero slip speed $v_r = 0$ (i.e., $s = 0$):

$$F_{x,y}(s \approx 0) = L\sigma_{0x,y} \frac{v_{rx,y}}{|r\omega|} \left[\frac{1}{2!} - \frac{1}{3!} \frac{L\sigma_{0x,y}}{g(v_r)} \frac{|v_r|}{|r\omega|} + \frac{1}{4!} \frac{L^2\sigma_{0x,y}^2}{g^2(v_r)} \frac{|v_r|^2}{|r\omega|^2} \mp \dots \right] + \sigma_2 v_{rx,y}. \quad (26)$$

Equation (26) is useful for calculating the longitudinal/lateral tire stiffness which is defined [3] as the zero-slip slope of the tire static curves:⁵

$$K_{x,y} = \left[\lim_{s \rightarrow 0} \left| \frac{dF_x}{ds} \right|_{\alpha=0} \quad \lim_{\alpha \rightarrow 0} \left| \frac{dF_x}{d\alpha} \right|_{s=0} \right] = \frac{1}{2} L\sigma_{0x,y}. \quad (27a)$$

Similarly, the aligning stiffness is found to be

$$K_z = \lim_{\alpha \rightarrow 0} \left| \frac{d(-M_z)}{d\alpha} \right|_{s=0} = \frac{1}{12} L^2 \sigma_{0y}. \quad (27b)$$

Based on the result (27a), and the fact that the tire forces tend to the sliding friction force $g(v_r)$ for large slip speeds v_r and $\sigma_2 \approx 0$ (i.e., for $s \rightarrow 1 \Rightarrow Z_{x(y)} \rightarrow 0$; Eq. (25a)), the tire force static curves can be constructed as illustrated in Figure 6.

Instead of the uniform longitudinal normal pressure distribution, a more realistic **non-uniform pressure distribution** may be used to obtain a more accurate tire friction model. According to the experimental results presented in [32, 33] and discussions in [1, 3, 21], the longitudinal normal pressure distribution $\hat{p}(\zeta)$ may conveniently be described by the asymmetric trapezoidal function shown in Figure 7. By taking into account Equation (19), the magnitude of the normalized pressure distribution $\hat{p}(\zeta)$ is found to be

$$\hat{p}_m = \frac{2}{1 + r_r - r_l}, \quad (28)$$

with the relative left and right margins of the trapezoidal distribution defined as (Fig. 7):

$$r_{l,r} = \frac{\zeta_{l,r}}{L}. \quad (29)$$

⁴A special case $v = r\omega = 0$ of the pure rolling singularity at $v_r = 0$ is treated in Section 6.

⁵The term $\sigma_2 v_{rx,y}$ in Equation (26) is neglected in Equation (27), since $0.5L\sigma_{0x,y} \gg \sigma_2 |r\omega|$.

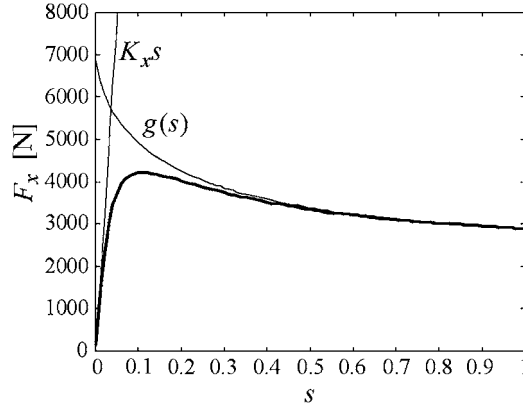


Fig. 6. Construction of LuGre model static curve for pure longitudinal motion.

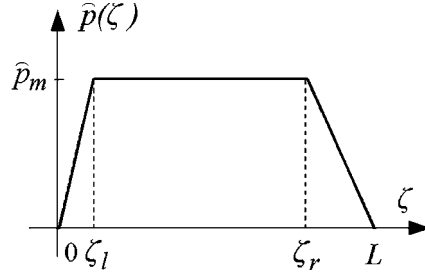


Fig. 7. Asymmetric trapezoidal normal pressure distribution.

Solving the integral Equations (20) and (21) on the intervals $[0, \zeta_l]$, $[\zeta_l, \zeta_r]$, and $[\zeta_r, L]$, and rearranging gives the following final expressions of the static model for non-uniform normal pressure distribution:

$$F_{x,y} = \frac{v_{rx,y}}{|v_r|} g(v_r) \left\{ 1 - \frac{2}{1 + r_r - r_l} \rho_{x,y} \left[\frac{\rho_{x,y}}{r_l} \left(1 - e^{-r_l/\rho_{x,y}} \right) - \frac{\rho_{x,y}}{1 - r_r} \left(e^{-r_r/\rho_{x,y}} - e^{-1/\rho_{x,y}} \right) \right] \right\} + \sigma_2 v_{rx,y}, \quad (30a)$$

$$M_z = \frac{v_{ry}}{|v_r|} g(v_r) \frac{L}{2} \left\{ 1 - K_v + \frac{2}{1 + r_r - r_l} \rho_y^2 \left[\frac{4\rho_y - 1}{r_l} - \frac{4\rho_y + 2r_l - 1}{r_l} e^{-r_l/\rho_y} - \frac{4\rho_y + 2r_r - 1}{1 - r_r} e^{-r_r/\rho_y} + \frac{4\rho_y + 1}{1 - r_r} e^{-1/\rho_y} \right] \right\} + \frac{L}{2} (1 - K_v) \sigma_2 v_{ry}, \quad (30b)$$

with

$$K_v = \frac{2}{L^2} \int_0^L \zeta \hat{p}(\zeta) d\zeta = \frac{2}{3} \frac{1 + r_r + r_r^2 - r_l^2}{1 + r_r - r_l} = \hat{p}_m \frac{1 + r_r + r_r^2 - r_l^2}{3}, \quad (31a)$$

$$\rho_{x,y} = \frac{Z_{x,y}}{L} = \frac{1}{L} \left| \frac{r\omega}{v_r} \right| \frac{g(v_r)}{\sigma_{0x,y}}. \quad (31b)$$

The stiffness coefficients for the model (30) are found to be:

$$K_{x,y} = \frac{1}{2} L \sigma_{0x,y} K_v, \quad (32a)$$

$$K_z = \frac{1}{6} L^2 \sigma_{0y} \frac{r_r^3 + r_l^2 - r_l^3}{1 + r_r - r_l}. \quad (32b)$$

5. LUMPED MODEL

The distributed dynamic tire friction model derived in Subsection 4.1 is characterized by a relatively complex finite-difference implementation and relatively low computing efficiency. Therefore, it would be convenient to transform it to a lumped-parameter form with only a few internal (lumped) states. The lumped model is derived for the case of asymmetric trapezoidal normal pressure distribution (Fig. 7). The final model for the special case of uniform normal pressure distribution is also presented.

5.1. Lumped Model for Longitudinal and Lateral Forces

The lumped model for longitudinal and lateral forces ($F_{x,y}$ -model) is defined in a pair of space-independent states $\tilde{z}_{x,y}(t)$, which are obtained by averaging the deflection variables $z_{x,y}(\zeta, t)$ weighted by the normalized normal pressure distribution $\hat{p}(\zeta)$:

$$\tilde{z}_{x,y}(t) \triangleq \frac{1}{L} \int_0^L z_{x,y}(\zeta, t) \hat{p}(\zeta) d\zeta. \quad (33)$$

Averaging the distributed $F_{x,y}$ -model, given by Equations (17), (18) and (20) (by applying the integral $\frac{1}{L} \int_0^L (\cdot) \hat{p}(\zeta) d\zeta$), and taking into account the lumped state

variables definition (33) yields

$$\frac{d\tilde{z}_{x,y}(t)}{dt} = v_{rx,y} - \frac{\sigma_{0x,y}|v_r|}{g(v_r)}\tilde{z}_{x,y}(t) - \frac{r|\omega|}{L}S_{x,y}(t), \quad (34a)$$

$$F_{x,y}(t) = \sigma_{0x,y}\tilde{z}_{x,y}(t) + \sigma_{1(x,y)}\frac{d\tilde{z}_{x,y}(t)}{dt} + \sigma_2v_{rx,y}, \quad (34b)$$

with

$$S_{x,y}(t) = \int_0^L \frac{\partial z_{x,y}(\zeta, t)}{\partial \zeta} \hat{p}(\zeta) d\zeta. \quad (35)$$

All the terms in the model (34), except the term $S_{x,y}$ (Eq. (35)), have the lumped forms. The integral expression (35) can be solved by using the finite difference method, as shown in [23]. The final solution is

$$S_{x,y}(t) = \hat{p}_m \left(\frac{1}{L - \zeta_r} \int_{\zeta_r}^L z_{x,y}(\zeta, t) d\zeta - \frac{1}{\zeta_l} \int_0^{\zeta_l} z_{x,y}(\zeta, t) d\zeta \right). \quad (36)$$

In order to obtain a lumped model, the terms $S_{x,y}(t)$ need to be approximately expressed as functions of the lumped state variables $\tilde{z}_{x,y}(t)$. The simple linear relation between these variables has been proposed in [19, 20]:

$$S_{x,y}(t) \approx \kappa_{x,y}\tilde{z}_{x,y}(t). \quad (37)$$

Hence, the state Equation (34a) assumes the following lumped form:

$$\frac{d\tilde{z}_{x,y}(t)}{dt} = v_{rx,y} - \left[\frac{\sigma_{0x,y}|v_r|}{g(v_r)} + \frac{\kappa_{x,y}}{L}r|\omega| \right] \tilde{z}_{x,y}(t). \quad (38)$$

The tire static curves (steady-state behavior) of the lumped model will be equal to those of the distributed model if the variable factors $\kappa_{x,y}$ are used (cf. [19, 20]):

$$\kappa_{x,y} = \left. \frac{S_{x,y}}{\tilde{z}_{x,y}} \right|_{\text{steady state}} = \frac{\hat{p}_m \left(\frac{1}{L - \zeta_r} \int_{\zeta_r}^L z_{x,y}(\zeta) d\zeta - \frac{1}{\zeta_l} \int_0^{\zeta_l} z_{x,y}(\zeta) d\zeta \right)}{\frac{1}{L} \int_0^L z_{x,y}(\zeta) \hat{p}(\zeta) d\zeta}. \quad (39)$$

Inserting Equation (23) for the steady-state deflection variable space-distribution in Equation (39), solving the integral expressions, and rearranging yields

$$\kappa_{x,y} = \frac{1}{\frac{1}{p_m E} - \rho_{x,y}}, \quad (40)$$

with

$$E = \frac{\rho_{x,y}}{r_l} \left(1 - e^{-r_l/\rho_{x,y}}\right) - \frac{\rho_{x,y}}{1 - r_r} \left(e^{-r_r/\rho_{x,y}} - e^{-1/\rho_{x,y}}\right) \quad (41)$$

and $\rho_{x,y}$ defined by Equation (31b). The factors $\kappa_{x,y}$ monotonically decrease with increase of the slip speed v_r . The boundary values of the factors $\kappa_{x,y}$ are found to be:

$$\kappa_{\min} = \lim_{v_r \rightarrow \infty} \kappa_{x,y} = 0, \quad (42a)$$

$$\kappa_{\max} = \lim_{v_r \rightarrow 0} \kappa_{x,y} = \frac{2}{K_v} = 2 \frac{(1 + r_r - r_l)/2}{(1 + r_r + r_r^2 - r_l^2)/3}. \quad (42b)$$

In the special case of uniform normal pressure distribution ($r_l = 0$, $r_r = 1$), the factors $\kappa_{x,y}$ are given by [19, 20]:

$$\kappa_{x,y} = \frac{1 - e^{-L/Z_{x,y}}}{1 - \frac{Z_{x,y}}{L} (1 - e^{-L/Z_{x,y}})}. \quad (43)$$

The boundary values of these factors are $\kappa_{\min} = 1$ and $\kappa_{\max} = 2$.

For large slip speeds v_r (i.e., when the tire is spinning), the LuGre tire friction model given by Equations (38) and (34b) should reduce to the standard LuGre friction model (9) (given for a sliding pair, cf. Fig. 6). Hence, the factors $\kappa_{x,y}$ in Equation (38) should tend to zero for large v_r , as predicted by Equation (42a). The same result was, however, not predicted in the case of uniform normal pressure distribution ($\kappa_{\min} = 1$). Nevertheless, both models predict similar dynamic behavior, since in the large slip operating regime the second term in the square bracket in Equation (38) (so-called convective term) is much smaller (for any $\kappa \leq 1$) than the first term in the square bracket.

It has been demonstrated in [19–22] that the simple lumped model with constant factors $\kappa_{x,y} \approx 1.2$ can effectively be used instead of the model with variable factors $\kappa_{x,y}$ given by Equation (40) or Equation (43) (see also Section 6).

5.2. Lumped Model for Self Aligning Torque

In order to derive a lumped self aligning torque model, an additional lumped model state is introduced:

$$\psi(t) \triangleq \frac{2}{LL} \int_0^L \zeta z_y(\zeta, t) \hat{p}(\zeta) d\zeta. \quad (44)$$

Using the definitions (33) and (44), and Equations (18) and (31a), the self aligning torque model output Equation (21) is readily transformed to the lumped form

$$M_z(t) = \frac{L}{2} \left[\sigma_{0y} (\tilde{z}_y(t) - \psi(t)) + \sigma_{1(y)} \left(\frac{d\tilde{z}_y(t)}{dt} - \frac{d\psi(t)}{dt} \right) + (1 - K_v) \sigma_2 v_{ry} \right]. \quad (45)$$

On the other hand, averaging the distributed model lateral (y) state Equation (17) (by applying the integral $\frac{2}{L^2} \int_0^L \zeta(\cdot) \bar{p}(\zeta) d\zeta$), and taking into account the lumped state variable definition (44) and Equation (31a) yields

$$\frac{d\psi(t)}{dt} = K_v v_{ry} - \frac{\sigma_{0y} |v_r|}{g(v_r)} \psi(t) - \frac{2}{L} r |\omega| S(t) \quad (46)$$

with

$$S(t) = \frac{1}{L} \int_0^L \zeta \frac{\partial z_y(\zeta, t)}{\partial \zeta} \bar{p}(\zeta) d\zeta. \quad (47)$$

Solving the integral expression (47) in the discrete-space domain gives [23]:

$$S(t) = -\tilde{z}_y(t) + S^*(t) \quad (48)$$

with

$$S^*(t) = \frac{\bar{p}_m}{L} \left(\frac{1}{L - \zeta_r} \int_{\zeta_r}^L z_y(\zeta, t) \zeta d\zeta - \frac{1}{\zeta_l} \int_0^{\zeta_l} z_y(\zeta, t) \zeta d\zeta \right). \quad (49)$$

In order to obtain a lumped model, the term $S^*(t)$ needs to approximately be expressed as a function of the lumped model states $\psi(t)$ and $\tilde{z}_y(t)$. The following simple linear relation between these variables is proposed:

$$S^*(t) \approx \lambda_1 \psi(t) + \lambda_2 \tilde{z}_y(t). \quad (50)$$

Taking into account Equations (48) and (50), the self aligning torque state Equation (46) assumes the following lumped form:

$$\frac{d\psi(t)}{dt} = K_v v_{ry} - \left[\frac{\sigma_{0y} |v_r|}{g(v_r)} + \frac{2\lambda_1}{L} r |\omega| \right] \psi(t) + \frac{2}{L} (1 - \lambda_2) r |\omega| \tilde{z}_y(t). \quad (51)$$

The following special (basic) case of relation (50) was considered in [22]:

$$S^*(t) \approx \lambda \psi(t). \quad (52)$$

In this case, in order to provide the correct steady-state model behavior, the factor λ is obtained as

$$\lambda = \frac{S^*}{\psi} \Big|_{\text{steady state}} = \frac{\frac{\hat{p}_m}{L} \left(\frac{1}{L-\zeta_r} \int_{\zeta_r}^L z_y(\zeta) \zeta d\zeta - \frac{1}{\zeta_l} \int_0^{\zeta_l} z_y(\zeta) \zeta d\zeta \right)}{\frac{2}{L} \int_0^L \zeta z_y(\zeta) \hat{p}(\zeta) d\zeta}. \quad (53)$$

Inserting Equation (23) in Equation (53), solving the integral expressions, and rearranging yields

$$\lambda = \frac{1 + \hat{p}_m \rho_y \left[\frac{\rho_y}{r_l} - \frac{\rho_y + r_l}{r_l} e^{-r_l/\rho_y} - \frac{\rho_y + r_r}{1-r_r} e^{-r_r/\rho_y} + \frac{\rho_y + 1}{1-r_r} e^{-1/\rho_y} \right]}{K_v - 2 \hat{p}_m \rho_y^2 \left[\frac{2\rho_y}{r_l} - \frac{2\rho_y + r_l}{r_l} e^{-r_l/\rho_y} - \frac{2\rho_y + r_r}{1-r_r} e^{-r_r/\rho_y} + \frac{2\rho_y + 1}{1-r_r} e^{-1/\rho_y} \right]}. \quad (54)$$

The factor λ monotonically decreases with increase of the slip speed v_r , where the boundary values are found to be

$$\lambda_{\min} = \lim_{v_r \rightarrow \infty} \lambda = \frac{1}{K_v}, \quad (55a)$$

$$\lambda_{\max} = \lim_{v_r \rightarrow 0} \lambda = \frac{3}{2} \frac{(r_r^2 + r_r + 1 - r_l^2)/3}{(r_r^3 + r_r^2 + r_r + 1 - r_l^3)/4}. \quad (55b)$$

If the more general relation (50) is used instead of Equation (52), one of the factors λ_1 and λ_2 can be fixed to an arbitrary constant value. It has been shown by simulation, that better results are obtained if the factor λ_2 is fixed to a constant value, with the factor λ_1 calculated to obtain the correct steady-state behavior:

$$\lambda_1 = \frac{L}{2} \frac{1}{r|\omega|} \left[\frac{\frac{2}{L}(1 - \lambda_2)r|\omega|\tilde{z}_y + K_v v_{ry}}{\frac{2}{L}r|\omega|\tilde{z}_y + K_v v_{ry}} \left(\frac{\sigma_{0y}|v_r|}{g(v_r)} + \frac{2\lambda}{L}r|\omega| \right) - \frac{\sigma_{0y}|v_r|}{g(v_r)} \right]. \quad (56)$$

In the special case of uniform normal pressure distribution ($r_l = 0$, $r_r = 1$) [22], the factor λ is given by

$$\lambda = \frac{1 - e^{-L/Z_y}}{1 + 2 \frac{Z_y}{L} e^{-L/Z_y} - 2 \frac{Z_y^2}{L^2} (1 - e^{-L/Z_y})}. \quad (57)$$

Its boundary values λ_{\min} and λ_{\max} take on the values 1 and 1.5, respectively. Note that the constant K_v in the state Equation (51) becomes equal to 1.

The final lumped tire friction model is given by the state Equations (38) and (51), the output Equations (34b) and (45), and the algebraic Equations (40), (54),

and (56) for the specific lumped model parameters $\kappa_{x,y}$, λ , and λ_1 . It should be noted that, unlike the first-order longitudinal/lateral force model, the self aligning torque model is of second order ($\dot{\psi}$ in Eq. (51) is function of both ψ and \ddot{z}_y ; cf. [9, 11]).

6. VALIDATION OF TIRE FRICTION MODEL

The steady-state behavior of the developed LuGre dynamic tire friction model is validated with respect to “magic” formula static model presented in [5, 6]. The dynamic behavior of the lumped model is validated by comparing its time responses with the distributed model responses. Comparative results of computing efficiencies of the static and lumped-dynamic versions of the LuGre tire friction model are also included.

6.1. Validation of Steady-state Behavior

The “magic” formula model is used as a benchmark, because it can accurately describe the tire static curves [5, 6]. The basic form of the “magic” formula model is considered, which does not include the horizontal and vertical shifts of the tire static curves ($S_h = S_v = 0$ in Table 1 in [5]). The normal force is $F_z = 4000$ N. The LuGre model parameters have been numerically optimized with respect to the “magic” formula model static curves for pure braking and pure cornering. The optimized parameters are listed in Appendix A.

Figure 8 shows that the optimized LuGre model with the uniform normal pressure distribution predicts very similar pure braking/cornering tire static curves as the “magic” formula model. A good agreement between the curves predicted by the LuGre and “magic” formula models is observed in the more complex task of combined braking and cornering as well (Fig. 9). The maximum error of longitudinal/lateral force prediction is 4% of maximum tire force. Figure 10 indicates that the simple lumped LuGre model with the constant factor $\kappa_{x,y} = 1.2$ has similar steady-state curves as the distributed model (or lumped model with variable $\kappa_{x,y}$), especially at larger slips s and α .

Figure 11 shows that the self aligning torque characteristic for pure cornering significantly differs from one predicted by the “magic” formula model. This difference is primarily a consequence of the assumed uniform normal pressure distribution [21]. By using the asymmetric trapezoidal normal pressure distribution from Figure 7, the accuracy of the self aligning torque prediction is significantly improved, including a correct prediction of change of sign of self aligning torque for large slip angles (Fig. 11). However, the prediction error is still larger than the corresponding error of prediction of the longitudinal/lateral force curves. The force model accuracy is practically not influenced by the introduction of non-uniform pressure distribution ([21, 22], Section 8).

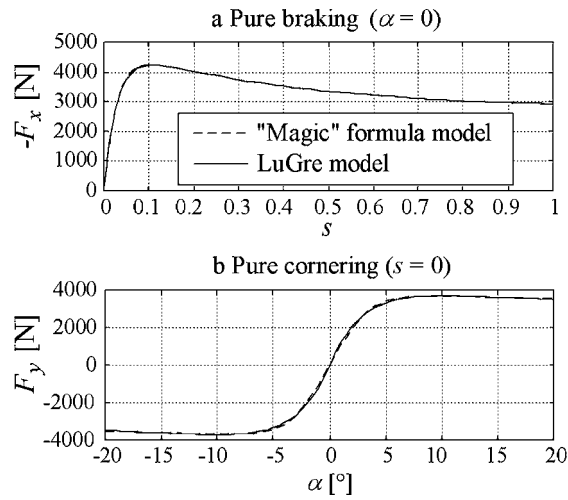


Fig. 8. Tire static characteristics for pure braking (a) and pure cornering (b) obtained from “magic” formula and LuGre models.

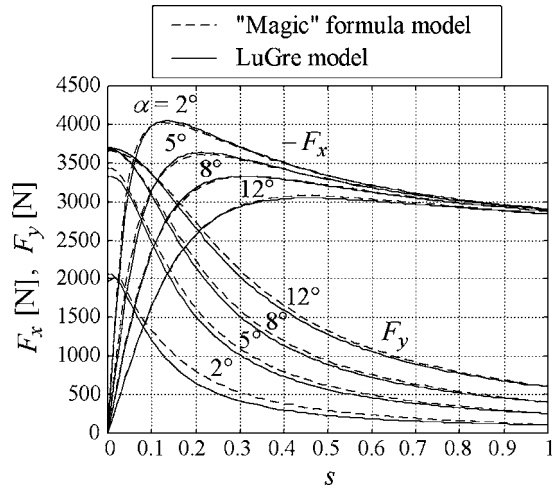


Fig. 9. Tire static characteristics for combined braking and cornering obtained from “magic” formula and LuGre models.

The self aligning torque validation results for combined longitudinal and lateral motion will be included in Section 7 (Fig. 20), after an empirical extension of the model is first introduced.

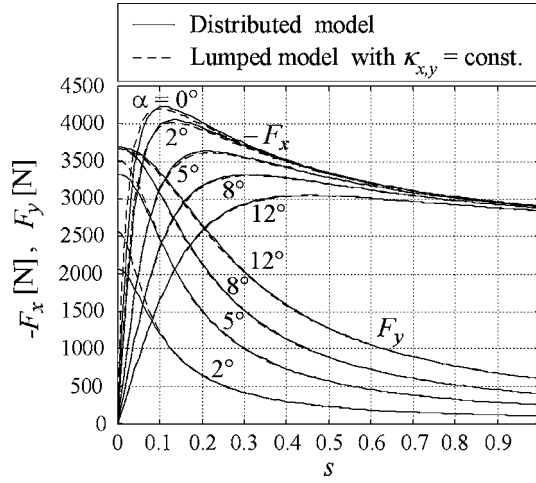


Fig. 10. Tire static characteristics for distributed LuGre model and corresponding lumped model with constant factor $\kappa_{x,y} = 1.2$.

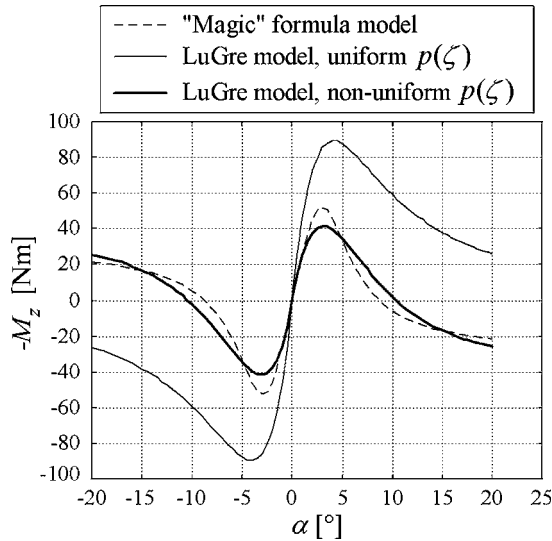


Fig. 11. Self-aligning torque static curves for pure cornering obtained from "magic" formula and LuGre models.

6.2. Validation of Dynamic Behavior

Figure 12 shows the comparative pure-braking step responses of an elementary one-wheel vehicle model [19, 20] with the LuGre tire friction model given in the

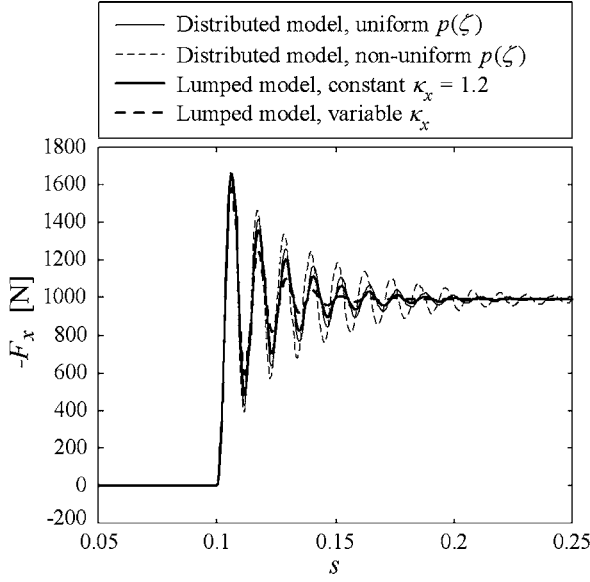


Fig. 12. Step response of simple vehicle model with distributed and lumped tire models ($\sigma_1 = 0$).

distributed and lumped forms for the uniform and non-uniform normal pressure distributions. The tire sidewall compliance is not included in the model (Section 2). Thus, the tire force oscillations observed in Figure 12 are due to tire tread dynamics. The response of the lumped model with constant factor $\kappa_x = 1.2$ is in a good agreement with the original distributed model response. If the variable factor κ_x is used (in order to provide the exact match of the distributed model static curves), the dynamic response accuracy is worsen somewhat compared to the use of constant κ_x . Figure 12 also illustrates that the dynamic responses of the tire models with uniform and non-uniform normal pressure distributions are very similar.

Figure 13 shows comparative responses of the lumped and distributed LuGre tire models to a series of slip angle steps during pure cornering, where the basic form of the self aligning torque model with $\lambda_1 = \lambda$ and $\lambda_2 = 0$ is used. Figure 14 shows the comparative responses for different wheel center speeds v . Evidently, the lumped model responses preserve all basic characteristics of the original distributed model, which include:

- A characteristic inflexion point of the self aligning torque response, which does not appear in the lateral force response (note that this difference is due to different orders of the $F_{x,y}$ and M_z -models, Section 5).

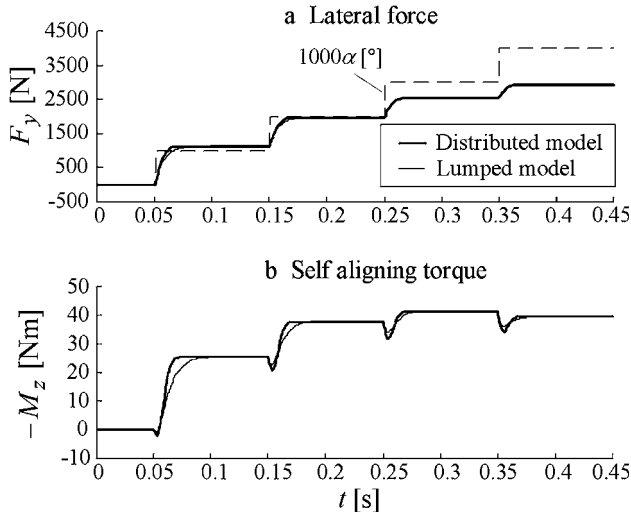


Fig. 13. Comparative pure cornering step responses of distributed and lumped tire models ($\lambda_2 = 0$).

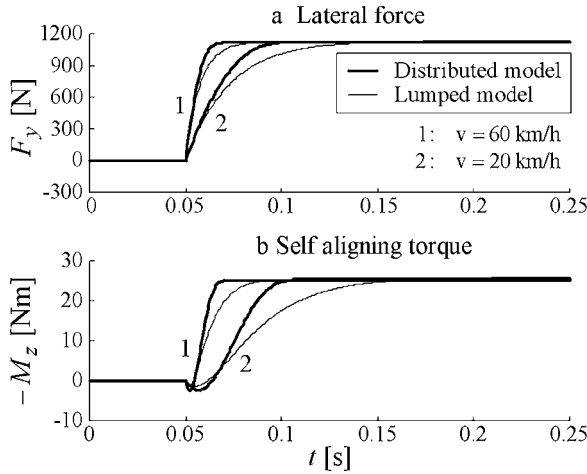


Fig. 14. Comparative pure cornering step responses for different wheel center speeds ($\alpha: 0 \rightarrow 1^\circ$ at 0.05 s).

- A characteristic initial undershoot of the self-aligning torque response. This effect reveals a non-minimum-phase nature of the M_z -model.
- Slow-down of the model response with decrease of the wheel speed. This effect may imply that the tire friction dynamics has larger impact to vehicle dynamics at lower vehicle speeds.

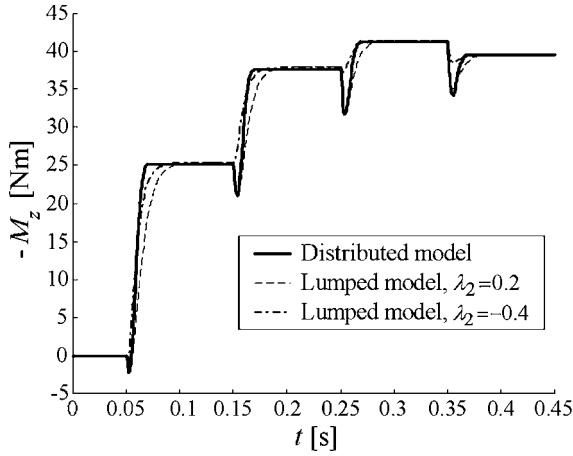


Fig. 15. Comparative pure cornering step responses for different factors λ_2 .

However, the lumped model response is slower than the response of the distributed model, particularly at lower slip angles α (up to 10% slower for F_y and up to 40% slower for M_z , according to the results of application of the flexion-tangent identification method).

Figure 15 illustrates the effects of introducing the factor $\lambda_2 \neq 0$ in the lumped form of self aligning torque model. This factor influences the initial delay (equivalent dead-time) and initial undershoot of the self aligning torque step response. The lumped model with $\lambda_2 = 0.2$ predicts more accurate initial part of the response compared to the basic lumped model with $\lambda_2 = 0$, while the choice $\lambda_2 = -0.4$ provides more accurate response settling time (cf. Figs. 15 and 13). Hence, the factor λ_2 can effectively be used to tune the lumped model with respect to experimentally observed tire friction dynamic behavior.

6.3. Test of Computing Efficiency

Computing efficiency of the LuGre tire friction model given in static and lumped-dynamics forms is examined on the example of a simple one-wheel vehicle model [19, 20]. The comparative computing efficiency tests are performed for different vehicle speeds. The model is excited by a stepwise braking torque at large vehicle speeds, and a zero-offset sine wheel torque at low speeds [24].

The test results, given in Table 1 [24], show that the computing efficiency of the static model is significantly deteriorated at low vehicle speeds. On the other hand, the dynamic LuGre model has the same, good computing efficiency over the whole speed range. It is thus capable to efficiently handle zero-vehicle-speed simulations, for

Table 1. Comparative simulation execution times for a simple vehicle model with static and dynamic LuGre models.

Tire model	Simulation time [0.1 s]						
	τ -form v_0 [m/s]	Step 40	Step 20	Step 5	Sine 5	Sine 1	Sine 0.2
Static model		1.09	1.05	1.48	2.53	10.72	39.11
Dynamic model		1.16	1.15	1.16	1.15	1.15	1.21

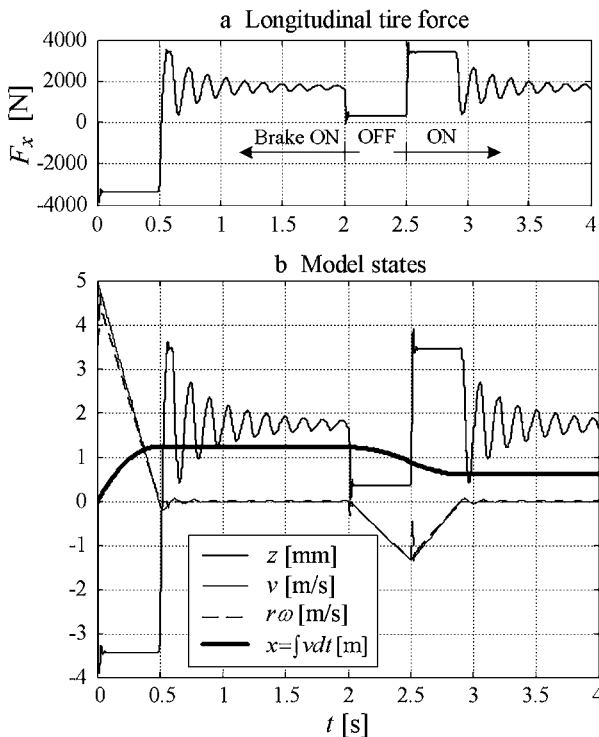


Fig. 16. Simulation response of simple vehicle model with lumped LuGre tire model during braking on hill.

which the static model (i.e., the slip s) is even not defined. This is illustrated by a braking-on-hill simulation response shown in Figure 16 [24].

The inferior low-speed computing performance of the static model is explained by the static tire curves shown in Figure 17. When expressed in the relative speed v_r (rather than in the slip s), the tire static curves become stiffer in the low-slip (adhesion) region

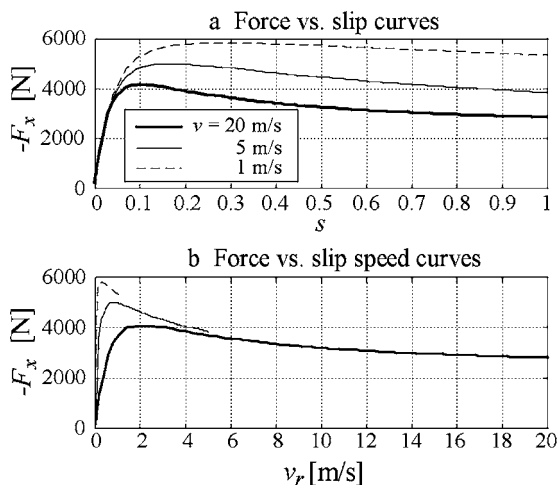


Fig. 17. Static tire curves as functions of slip s (a) and slip speed v_r (b).

as the vehicle speed decreases. This leads to the stiff simulation problem, and finally results in the large simulation time. The problem is similar to the well-known problem of low computing efficiency of the classical sliding bearing friction model (Fig. 4a) with steep straight-line approximation of zero-speed friction (stiction) [14, 37].

7. SOME EMPIRICAL EXTENSIONS OF STATIC MODEL

It has been demonstrated in the previous section that a relatively simple LuGre model with only three internal states and up to ten parameters can provide quite accurate description of the 3D tire friction static and dynamic behavior. In order to further enhance the model accuracy, some physical and empirical model extensions are proposed in this section.

7.1. Sliding Friction Dependence on Slip Vector Orientation Angle

It is generally recognized that the parameters of friction curve $g(v_r)$ (Eq. (6)) depend on the motion directions [34, 35]. This observation may be extended for the two-dimensional (x - y) motion of friction element, in the way that friction parameters are made linearly dependent on the orientation angle β of the relative speed (slip) vector $\vec{v}_r = v_{rx} + jv_{ry}$ [1]:

$$\beta = \text{atan}(|v_{ry}/v_{rx}|). \quad (58)$$

If the parameters of the original sliding friction function (6) are defined for pure longitudinal motion ($g_{x0}(v_r) = F_C + (F_S - F_C)e^{-|v_r/v_s|^\delta}$), and if the corresponding friction function for pure lateral motion is expressed as $g_{y0}(v_r) = G_y g_{x0}(v_r)$, the sliding friction function for combined longitudinal and lateral motion can be calculated as

$$g(v_r) = \left(1 + \frac{G_y - 1}{\pi/2}\beta\right) g_{x0}(v_r) = \left(1 + \frac{G_y - 1}{\pi/2}\beta\right) \left[F_C + (F_S - F_C)e^{-|v_r/v_s|^\delta}\right]. \quad (59)$$

It is demonstrated in [25] that introduction of the model parameter $G_y \approx 1$ provides independent tuning of high-slip (sliding) and low-slip (adhesion) parts of pure braking/cornering tire curves, thus increasing the model accuracy.

7.2. Correction of Tire Force Model for Combined Longitudinal and Lateral Motion

The validation results shown in Figure 9 have demonstrated good accuracy of the LuGre static model for combined longitudinal and lateral motion. Modeling errors are only evident for the lateral force (F_y) curves in the medium/high-slip region. The medium/high-slip parts of the lateral force curves are influenced by the lateral component of sliding friction function, $g_y = |v_{ry}/v_r|g(v_r)$ (cf. Fig. 6, and Eqs. (16) and (25a)). The underestimated lateral forces in Figure 9 are, thus, consequence of underestimated friction function g_y (see [25] for illustration).

The lateral force model accuracy can be increased by increasing the function g_y in the medium/large slip region $s > 0.2$. Since g_y is proportional to $|v_{ry}|$, and since v_{ry} is proportional to $\sin(\alpha)$ (Eq. (3)), the function g_y can be increased by adding a shift $\Delta\alpha_y \text{sgn}(\alpha)$ to the slip angle α when calculating v_{ry} . In other words, the function g_y should be scaled by the factor $\sin(\alpha + \Delta\alpha_y \text{sgn}(\alpha))/\sin(\alpha) \approx (\alpha + \Delta\alpha_y \text{sgn}(\alpha))/\alpha = 1 + \Delta\alpha_y/|\alpha|$. Since F_y is proportional to g_y , the lateral force model can simply be scaled by the correction factor

$$\frac{F_y}{F_{y0}} = \begin{cases} 1 + \frac{\Delta\alpha_y \min(s, 0.2)}{|\alpha|}, & \text{for } |\alpha| > \alpha_{0y} \\ 1, & \text{otherwise} \end{cases}. \quad (60)$$

The scaling is not performed for very small slip angles $|\alpha| < \alpha_{0y}$, in order to avoid division by zero.

Figure 18, when compared with Figure 9, shows that the introduction of correction (60) significantly improves the accuracy of the static LuGre model.

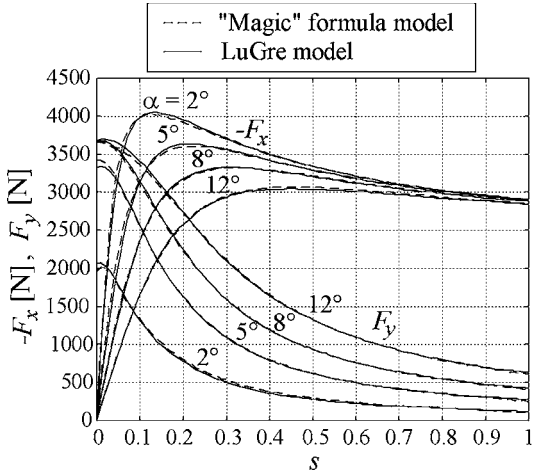


Fig. 18. LuGre tire model static curves after steady-state model extension, and “magic” formula model curves.

7.3. Correction of Self Aligning Torque Model

The accuracy of self aligning torque static curves shown in Figure 11 can be increased by using a slip-dependent right margin of the trapezoidal normal pressure distribution $r_r(\alpha)$ [25]. Figure 19 shows the “ideal” curve $r_r(\alpha)$ which gives zero error of self aligning torque modeling. This curve may be interpolated by using the “magic” formula from [5], as will be demonstrated in Section 8.

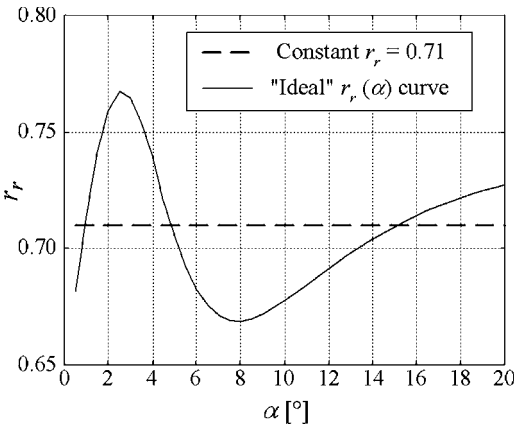


Fig. 19. Normal pressure distribution right margin vs. slip angle curve for exact match of self aligning torque curve.

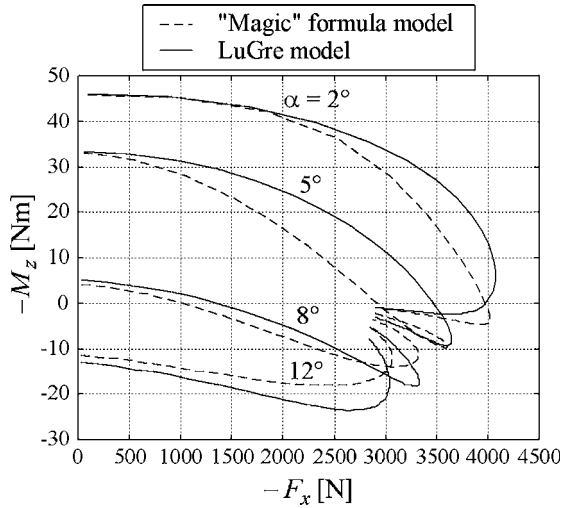


Fig. 20. Self aligning torque static curves for combined braking and cornering obtained from “magic” formula and LuGre models.

Figure 20 shows the static curves of the corrected self aligning torque model for combined braking and cornering. The main difference compared to the “magic” formula model is a lower rate of decrease of torque with the longitudinal force increase. However, it is important to note that the “magic” formula model curves themselves were not in entirely good agreement with the experimental results (see Figs. 23 and 24 in [5]), and also that appears that the LuGre model describes the experimental results in [5] more accurately.

8. MODEL PARAMETERIZATION

The tire parameters are highly dependent on different tire/road conditions, such as normal force F_z , road condition (e.g., dry or wet asphalt), and tire pressure. This section presents parameterization and validation of the 3D LuGre tire friction model with respect to normal force. Qualitative parameterization of the model for other tire/road conditions is also discussed.

8.1. Parameterization With Respect to Normal Force

It is well known that both adhesion and sliding parts of static tire curves (cf. Fig. 6) depend on the normal force F_z (see e.g. [1, 3, 21]). Since these relationships are

roughly proportional, it is convenient to rewrite the friction function $g(v_r)$ and the normalized space constants $\rho_{x,y}$ to:

$$\bar{g}(v_r) = \frac{g(v_r)}{F_z} = \left(1 + \frac{G_y - 1}{\pi/2} \beta\right) \bar{g}_{x0}(v_r) = \left(1 + \frac{G_y - 1}{\pi/2} \beta\right) \left[\mu_C + (\mu_S - \mu_C) e^{-|v_r/v_s|^\delta}\right], \quad (61)$$

$$\rho_{x,y} = \frac{Z_{x,y}}{L} = \frac{1}{L} \left| \frac{r\omega}{v_r} \right| \frac{g(v_r)}{\sigma_{0x,y}} = \left| \frac{r\omega}{v_r} \right| \frac{\bar{g}(v_r)}{k_{x,y}}, \quad (62)$$

where $\mu_C = F_C/F_z$ and $\mu_S = F_S/F_z$ are the friction coefficients, and $k_{x,y}$ are the normalized tire stiffness coefficients given by

$$k_{x,y} = L \frac{\sigma_{0x,y}}{F_z}. \quad (63)$$

The parameters of the static LuGre model are optimized with respect to “magic” formula static model documented in [5, 6]. The optimization is performed in the following steps.

- 1) *Optimization of 2D model parameters.* The basic model parameters $k_{x,y}$, μ_C , μ_S , and G_y are initially optimized with respect to pure braking/cornering tire force static curves for the uniform normal pressure distribution (Eqs. (25a) and (61)–(63)) [26]. The Stribeck parameters v_s and δ , and the viscous friction coefficient σ_2 have been found approximately independent of the normal force [21], so that they are set to constant values (Appendix B.1).

According to Equation (63), three model parameters $\sigma_{0x,y}$ and L should be calculated from two optimized parameters $k_{x,y}$. This means that one of the three model parameters should be related to the other two parameters. According to the discussion in Subsection 3.3, it is reasonable to assume the proportional σ_{0x} vs. F_z dependence, namely $\sigma_{0x} = \bar{\sigma}_{0x} F_z$, where $\bar{\sigma}_{0x}$ is determined from Equation (63) based on the assumption that $L = 0.25$ m for $F_z = 4$ kN. The contact patch length vs. normal force dependence $L(F_z) = k_x(F_z)/\bar{\sigma}_{0x}$ can then be accurately described by [33]

$$L(F_z) = a + b\sqrt{F_z}. \quad (64)$$

And finally, the function $\sigma_{0y}(F_z) = k_y F_z / L(F_z)$ is interpolated by a second-order polynomial. The fact that the lateral stiffness σ_{0y} is not a linear function of the normal force F_z may be explained by the influence of lateral sidewall compliance.

Figure 21 demonstrates a high accuracy of fitting the pure braking/cornering tire force curves by the 2D LuGre model with the optimized (and interpolated) parameters given in Appendix B.1. A slight disagreement of the F_y curve for

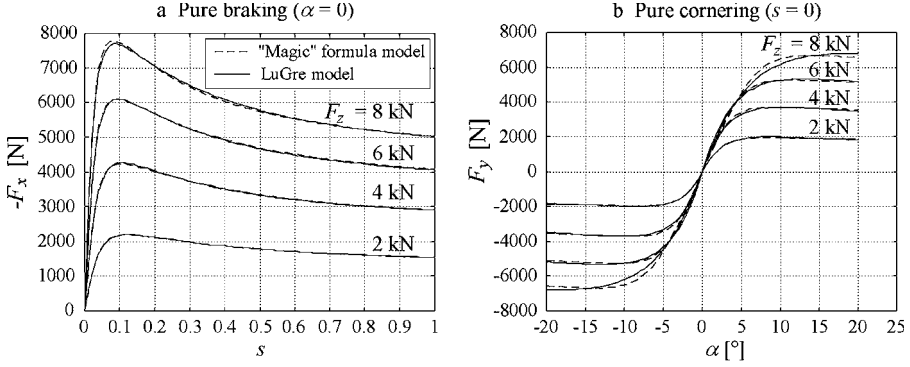


Fig. 21. Optimized pure braking and pure cornering curves for different normal forces.

$F_z = 8$ kN is primarily a consequence of certain inaccuracy of straight-line interpolation of the optimized coefficient $\mu_s(F_z)$.

- 2) *Optimization of 3D model parameters.* The basic parameterization from Point (1) is extended for the case of 3D model which includes the self aligning torque sub-model. The asymmetric trapezoidal normal pressure distribution is considered (see Eq. (30)). As in the case of $F_{x,y}$ model, the experimental results in [32, p. 683] confirm approximately proportional relation between M_z and F_z implied by Equation (30b). However, this is not the case with the experimental results from [5, 6], which are used here as a basis for the LuGre tire model parameterization. Therefore, the self aligning torque relation (30b) is scaled by an empirical factor ϕ , which is also optimized as a function of the normal force F_z . The optimization starts with initial values of parameters $k_{x,y}$, μ_C , μ_S , and G_y optimized in Point (1), and includes the additional parameters r_l , r_r , and ϕ .
- 3) *Optimization of slip angle-dependence of parameter r_r .* The empirical dependence $r_r(\alpha)$ (Section 7) is optimized for different normal forces F_z . These “ideal” $r_r(\alpha)$ curves are shown in Figure 22. When shifted along the vertical axis, they become quite similar. This means that all these curves (represented by the averaged curve $\bar{r}_r(\alpha)$) may be described by a single constant-parameter dependence with variable vertical shift. The “magic” formula [5] is used here for this purpose:

$$r_r(\alpha) = D \sin(C \arctan(B((1 - E)|\alpha| + (E/B)\arctan(B|\alpha|)))) + S_v(F_z). \quad (65)$$

The validation results of the self aligning torque model with optimized function $r_r(\alpha)$ (Appendix B.2) are shown in Figure 23. Introduction of the variable margin r_r improves the shape of the curves and the accuracy of the peak value (cf. Figs. 23 and 11). However, the accuracy of the self aligning torque model is still significantly lower than the accuracy of the force model.

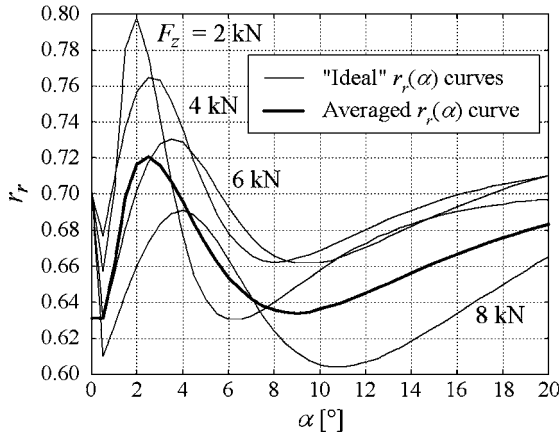


Fig. 22. Optimal right margin parameter curves $r_r(\alpha)$ for different normal forces.

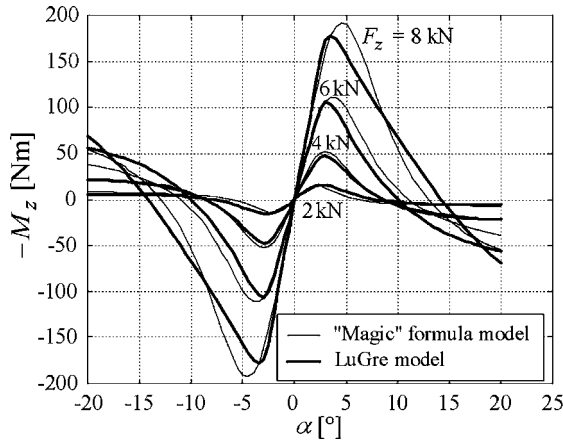


Fig. 23. Pure-cornering self aligning torque curves for different normal forces and for variable normal pressure distribution parameter $r_r(\alpha)$.

- 4) *Re-optimization of 3D model parameters.* The 3D model parameters are re-optimized taking into account the function $r_r(\alpha)$ optimized in Point (3). The parameter r_l is fixed to 0.15, since the self aligning torque curves are quite insensitive to this parameter.
- 5) *Interpolation of optimized parameters.* The optimized model parameter values are interpolated by the polynomials of the first or second order.

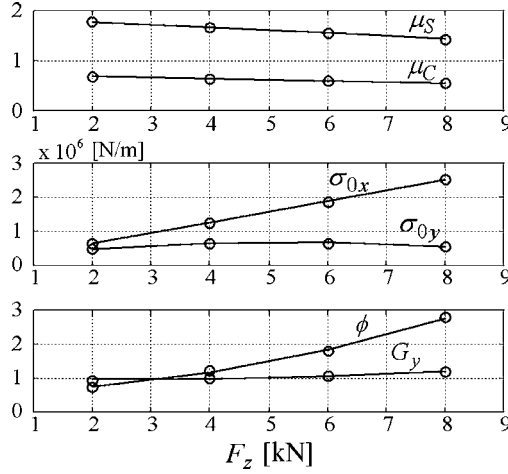


Fig. 24. Interpolation of 3D model parameters by 1st-order and 2nd-order polynomials.

Figure 24 shows the optimized and interpolated model parameters. Appendix B.2 includes the final equations for 3D model parameters as functions of the normal force.

The parameterized 2D and 3D models have been validated in [26, 27] for the case of combined longitudinal and lateral motion as well. The model accuracy was found to be comparable to that demonstrated in Section 6 for $F_z = 4$ kN (Figs. 9 and 20). A notable discrepancy was observed for $F_z = 8$ kN only; however, it was apparently caused more by inaccuracy of “magic” formula model implementation (due to incomplete data/documentation in [5, 6]) than by inaccuracy of the LuGre model itself.

8.2. Parameterization With Respect to Road Condition

The change of road condition (e.g. dry asphalt to ice transition) influences the parameters μ_C and μ_S of the sliding friction function $g(v_r)$. It appears appropriate to characterize the road condition by a single parameter μ_{sl} which scales the nominal sliding friction function g_0 valid for dry asphalt condition [18]:

$$g(v_r, \mu_{sl}) = \mu_{sl} g_0(v_r). \quad (66)$$

Typical values of the road condition coefficient μ_{sl} would be 1, 0.6, 0.2, and 0.1, for dry asphalt, wet asphalt, snow, and ice, respectively. Note that, in the general case, the individual parameters μ_C and μ_S of the sliding friction function g (Eq. (61)) should be scaled by different road condition-dependent coefficients. For example, the ratio μ_S/μ_C can be significantly higher for wet asphalt than for dry asphalt.

Equation (27a) implies that the friction coefficients μ_C and μ_S do not influence the low-slip (adhesion) portion of the tire curves. However, the experimental results in

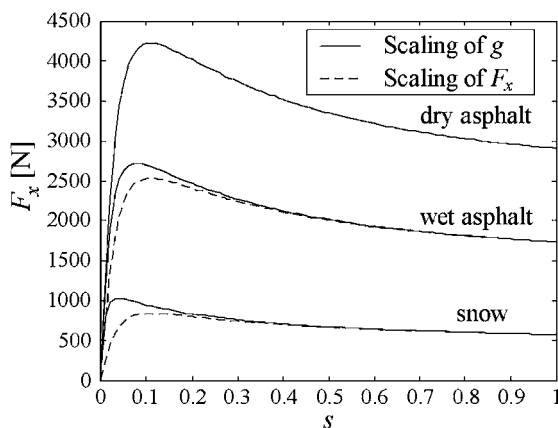


Fig. 25. Tire static curves for different road conditions.

[42–46] have shown opposite: the low-slip slope of the $F_x(s)$ curve (and the $F_y(\alpha)$ curve in [46]) depends on the road condition. This fact has been extensively used for road condition estimation [42–45]. According to the experimental results in [46], the low-slip slope is proportional to the sliding friction coefficient μ_{sl} . In order to include this effect in the LuGre model, the stiffness coefficients $\sigma_{0x,y}$ may be made linearly dependent on the road condition:⁶

$$\sigma_{0x,y}(\mu_{sl}) = \mu_{sl}\sigma_{0x,y0}. \quad (67)$$

Inserting Equations (66) and (67) in the static model given by Equations (25) or (30), and taking into account Equation (24), shows that the road condition should be introduced in the model by scaling the total tire friction functions $F_{x,y}$ and M_z by the road condition coefficient μ_{sl} , rather than scaling the sliding friction function $g(v_r)$ only. Figure 25 illustrates the longitudinal force static curves obtained by both methods.

It has been shown in [42, 43] that the low-slip slope of the $F_x(s)$ curve depends on the tire road condition only up to a certain sliding friction coefficient which is equal to approximately 0.3. In other words, the slope is different for dry asphalt and ice/snow, but not for dry and wet asphalt. In this case, the following saturated, road condition-dependence of the tire stiffness coefficients would be more appropriate than the linear dependence (67):

$$\sigma_{0x,y}(\mu_{sl}) = (1 - e^{-\mu_{sl}/0.3})\sigma_{0x,y0}. \quad (68)$$

⁶Note that according to Equation (27a), $F_{x,y}$ is proportional to the tire tread stiffness coefficients $\sigma_{0x,y}$ for the low-slip operation ($v_{rx,y} \rightarrow 0$; see also Fig. 6).

8.3. Influence of Other Tire/Road Conditions

There are three main tire model parameters/functions which are influenced by different tire/road conditions (Fig. 6): the stiffness coefficients $\sigma_{0,x,y}$, the sliding friction function $g(v_r)$, and the contact patch length L . The contact patch length is primarily important for the self aligning torque model, because it appears in this model independently of the stiffness coefficients (cf. Eqs. (25a) and (25b)).

The LuGre model inherently includes the dependence on the vehicle speed v . This dependence is demonstrated in Figure 17a, and it is in a good agreement with the experimental results presented in [47], although this dependence can vary quite a lot – especially for hydroplaning. The dependence on other tire/road condition parameters should be included in the model based on the experimental data [32, 33, 42, 47].

The tire inflation pressure primarily determines the tire stiffness and the contact length [32, Chap. 8], [33]. The higher the pressure, the larger is the stiffness and the lower is the contact length. The inflation pressure can also influence the sliding friction function $g(v_r)$; the rate of decrease of the function $g(v_r)$ is higher for lower pressures [32, p. 328].

The tire tread wear increases the tire stiffness [32, Chap. 8], [43]. On the other hand, the tire tread temperature increase lowers sliding friction [33]. Hydroplaning effect, caused by a high water cover depth at high vehicle speeds, also lowers sliding friction [47]. In addition, it decreases the tire static curve stiffness $K_{x,y}$ (Eq. (27a)) [43], as the consequence of decrease of the contact length L .

9. CONCLUSION

A 3D dynamic tire friction model for combined longitudinal and lateral motion has been developed based on the LuGre friction model. The model has been originally derived in the distributed brush form, and then transformed to a simple lumped form with three internal states. The model validation has shown that the use of uniform normal pressure distribution over the tire/road contact patch can yield accurate static and dynamic behaviors of the longitudinal and lateral forces (the 2D model). However, a more complex asymmetric non-uniform normal pressure distribution along the longitudinal axis is needed to predict accurate self aligning torque behavior (the 3D model).

The lumped model has the same static tire friction curves as the original distributed model if the variable expressions for the characteristic lumped model factors are used. For the sake of simplicity of the 2D lumped model, constant values of the characteristic factors can also be used, with no significant deterioration of the static model accuracy. With respect to dynamic behavior, the 3D lumped model preserves all the basic characteristics of the original distributed model. However, the lumped model time-responses tend to be slower compared to distributed model responses, particularly for the self aligning torque. Introducing a redundant characteristic factor

in the self aligning torque lumped model gives a convenience of arbitrary tuning the self aligning torque response delay.

Validation of the first-principle 3D tire friction model with up to 10 physical parameters has pointed out that the model can provide quite accurate prediction of the tire static curves. Due to its simplicity, such a model should be adequate for many vehicle dynamics simulation studies, particularly for those oriented to vehicle dynamics controller design. In order to further improve the model accuracy, some empirical model extensions have been proposed and validated. The model parameterization with respect to normal force has given simple relations for model parameters and accurate model static curves. Qualitative parameterization with respect to other tire-road conditions has also been considered.

The main characteristics of the developed tire friction model are: good accuracy (particularly for 2D model), capability to capture different aspects of dynamics friction behavior, simplicity (particularly for uniform normal pressure distribution), good computing efficiency for wide speed operation (including zero vehicle speed operating mode), and ease of parameterization for different tire-road conditions. Therefore, the model can be a good alternative to the relaxation-length dynamic tire friction model.

Future work can be directed to additional (preferably physical) model extensions with the aim to increase the model accuracy and to include additional effects such as the camber angle effect and similar. Next, more thorough validation and parameterization of the model should be carried out based on a comprehensive set of experimental data. And finally, future efforts should include some practical aspects of model application such as incorporation in complex multi-body tire models, use in real time simulations, and comparison with present commercially-available tire friction models.

ACKNOWLEDGEMENT

It is gratefully acknowledged that this work has been supported by the Ford Motor Company, and the Ministry of Science and Technology of the Republic of Croatia. The authors would also like to express their appreciation to Jadranko Matuško for his help in optimizing the tire friction model parameters with respect to normal force.

REFERENCES

1. Bernard, J.E., Segel, L. and Wild, R.E.: Tire Shear Force Generation During Combined Steering and Braking Maneuvers. *SAE Paper No. 770852*, 1977.
2. Sakai, H.: Study on Cornering Properties of Tire and Vehicle. *Tire Science and Technology (TSTCA)* 18 (1990), pp. 136–169.

3. Pacejka, H.B. and Sharp, R.S.: Shear Force Development by Pneumatic Tyres in Steady State Conditions: A Review of Modelling Aspects. *Vehicle Syst. Dyn.* 20 (1991), pp. 121–176.
4. Pacejka, H.B.: *Tyre and Vehicle Dynamics*. Butterworth-Heinemann, Oxford, 2002.
5. Bakker, E., Nyborg, L. and Pacejka, H.B.: Tyre Modelling for Use in Vehicle Dynamics Studies. *SAE Paper No. 870421*, 1987.
6. Bakker, E., Pacejka, H.B. and Lidner, L.: A New Tire Model With an Application in Vehicle Dynamics Studies. *SAE Paper No. 890087*, 1989.
7. van Zanten, A., Ruf, W.D. and Lutz, A.: Measurement and Simulation of Transient Tire Forces. *SAE Paper No. 890640*, 1989.
8. van Zanten, A.: Measurement and Simulation of Transient in Longitudinal and Lateral Tire Forces. *SAE Paper No. 900210*, 1990.
9. Maurice, J.P.: *Short Wavelength and Dynamic Tyre Behaviour Under Lateral and Combined Slip Conditions*. Ph.D. Thesis, TU Delft, Netherlands, 2000.
10. Bernard, J.E. and Clover, C.L.: Tire Modeling for Low-speed and High-speed Calculations. *SAE Paper No. 950311*, 1995.
11. Maurice, J.P., Berzeri, M. and Pacejka, H.B.: Pragmatic Tyre Model for Short Wavelength Side Slip Variations. *Vehicle Syst. Dyn.* 31 (1999), pp. 65–94.
12. Clover, C.L. and Bernard, J.E.: Longitudinal Tire Dynamics. *Vehicle Syst. Dyn.* 29 (1998), pp. 231–259.
13. Zegelaar, P.W.A.: *The Dynamic Response of Tyres to Brake Torque Variations and Road Unevennesses*. Ph.D. Thesis, TU Delft, Netherlands, 1998.
14. Haessig, D.A. and Friedland, B.: On the Modeling and Simulation of Friction. *ASME J. Dyn. Syst., Measure. Contr.* 113 (1991), pp. 354–362.
15. Bliman, P.A., Bonald, T. and Sorine, M.: Hysteresis Operators and Tyre Friction Models. Application to Vehicle Dynamic Simulation. *Zeitschrift für angewandte Mathematik und Mechanik* 76 (1996), pp. 309–312.
16. Bliman, P.A. and Sorine, M.: Easy-to-use Realistic Dry Friction Models for Automatic Control. In: *Proceedings of Third European Control Conference*. Rome, Italy, September 1995, pp. 3788–3794.
17. Canudas de Wit, C., Olsson, H., Åström, K.J. and Lischinsky, P.: A New Model for Control of Systems With Friction. *IEEE Trans. Autom. Contr.* 40 (1995), pp. 419–425.
18. Canudas de Wit, C. and Tsiotras, P.: Dynamic Tire Friction Models for Vehicle Traction Control. In: *Proceedings of 38th Conference on Decision and Control*. Phoenix, AZ, December 1999, pp. 3746–3751.
19. Deur, J., Asgari, J. and Hrovat, D.: *Modeling and Analysis of Longitudinal Tire Dynamics*. FRL Technical Report No. SRR-2000-0145, Ford Motor Company, Dearborn, MI, September 2000.
20. Deur, J.: Modeling and Analysis of Longitudinal Tire Dynamics Based on the LuGre Friction Model. In: *Proceedings of Third IFAC Workshop Advances in Automotive Control*, Karlsruhe, Germany, March 2001, pp. 101–106.
21. Deur, J., Asgari, J. and Hrovat, D.: *A Dynamic Tire Friction Model for Combined Longitudinal and Lateral Motion*. FRL Technical Report No. SRR-2001-0022, Ford Motor Company, Dearborn, MI, January 2001.
22. Deur, J., Asgari, J. and Hrovat, D.: A Dynamic Tire Friction Model for Combined Longitudinal and Lateral Motion. In: *Proceedings of 2001 ASME International Mechanical Engineering Congress and Exposition (IMECE 2001)*, Vol. 2, New York, NY, November 2001, CD-ROM.
23. Deur, J.: A Brush-type Dynamic Tire Friction Model for Non-uniform Normal Pressure Distribution. In: *Proceedings of 15th Triennial IFAC World Congress*, Barcelona, Spain, July 2002, CD-ROM.
24. Deur, J.: *Some Practical Aspects of Application of LuGre Tire Model*. Internal Memorandum 02/12/01, University of Zagreb, Croatia, February 2001.

25. Deur, J.: *Improvement of LuGre Tire Model Steady-state Behavior*. Internal Memorandum 03/12/01, University of Zagreb, Croatia, March 2001.
26. Deur, J.: *Parameterization of LuGre Tire Model for Different Normal Forces*. Internal Memorandum 03/26/01, University of Zagreb, Croatia, March 2001.
27. Deur, J.: *Parameterization of LuGre Self Aligning Torque Model*. Internal Memorandum 10/31/01, University of Zagreb, Croatia, October 2001.
28. <http://www.fsb.hr/acg>, web site of Automotive Control Group at the University of Zagreb, Croatia.
29. Canudas-de-Wit, C., Tsiotras, P., Velenis, E., Basset, M. and Gissinger, G.: Dynamic Friction Models for Road/Tire Longitudinal Interaction. *Vehicle Syst. Dyn.* 39 (2003), pp. 189–226.
30. Deur, J., Asgari, J. and Hrovat, D.: Comments on the Paper Dynamic Friction Models for Road/Tire Longitudinal Interaction, by Canudas-de-Wit et al., VSD, Vol. 39, No. 3, pp. 189–226. *Vehicle Syst. Dyn.* 40 (2003), pp. 373–374.
31. Claeys, X., Yi, J., Alvarez, L., Horowitz, R. and Canudas de Wit, C.: A New 3D Tire/Road Friction Model for Vehicle Control and Simulation. In: *Proceedings of 2001 ASME International Mechanical Engineering Congress and Exposition (IMECE 2001)*, Vol. 2, New York, NY, November 2001, CD-ROM.
32. Clark, S.K. (ed.): *Mechanics of Pneumatic Tires*. U.S. Department of Transportation, NHTSA, Washington, D.C., 1981.
33. Sakai, H.: Theoretical and Experimental Studies on the Dynamic Cornering Properties of Tyres. *Int. J. Veh. Des.* 2(1–4) (1981).
34. Armstrong-Hélouvry, B.: *Control of Machines With Friction*. Kluwer Academic Publishers, Boston, 1991.
35. Armstrong-Hélouvry, B., Dupont, P. and Canudas de Wit, C.: A Survey of Models, Analysis Tools and Compensation Methods for the Control of Machines With Friction. *Automatica* 30 (1994), pp. 1083–1138.
36. Hrovat, D. and Tobler, W.E.: Internal Documents of Simulation of Advanced E8 Transmission Shift. Ford Motor Company, 1981–1983.
37. Karnopp, D.: Computer Simulation of Stick-slip Friction in Mechanical Dynamic Systems. *ASME J. Dyn. Syst., Measure. Contr.* 107 (1985), pp. 100–103.
38. Dahl, P.R.: *A Solid Friction Model*. Aerospace Report No. TOR-0158(3107-18)-1. The Aerospace Corporation, El Segundo, CA, 1968.
39. Walrath, C.D.: Adaptive Bearing Friction Compensation Based on Recent Knowledge of Dynamic Friction. *Automatica* 20 (1984), pp. 717–727.
40. Canudas de Wit, C. and Lischinsky, P.: Adaptive Friction Compensation With Partially Known Dynamic Friction Model. *Int. J. Adaptive Contr. Signal Process.* 11 (1997), pp. 65–80.
41. Dahl, P.R.: Measurement of Solid Friction Parameters of Ball Bearings. In: *Proceedings of Sixth Annual Symp. on Incremental Motion, Control Systems and Devices*, University of Illinois, ILO, 1977, pp. 49–60.
42. Dieckmann, T.: Assessment of Road Grip by Way of Measured Wheel Variables. In: *Proceedings of the FISITA*, London, June 1992, pp. 75–81.
43. Dieckmann, T.: *Der Reifenschlupf als Indikator für das Kraftschlußpotential*. Dissertation, TU Hannover, 1992.
44. Ito, M., Yoshioka, K. and Saji, T.: Estimation of Road Surface Conditions Using Wheel Speed Behavior. *SAE Paper No.* 9438826, 1994.
45. Gustafsson, F.: Slip-based Tire-road Friction Estimation. *Automatica* 33 (1997), pp. 1087–1099.
46. Witte, B. and Zuurbier, J.: *Detection of the Friction Coefficient in a Running Vehicle and Measurement of Tire Parameters on Different Road Surfaces*. VDI Berichte Nr. 1224 (in German), 1995.
47. Harned, J.L., Johnston, L.E. and Scharpf, G.: Measurement of Tire Brake Force Characteristics as Related to Wheel Slip (Antilock) Control System Design. *SAE Paper No.* 690214, 1969.

APPENDIX

A. Basic Set of Model Parameters (for $F_z = 4$ kN, Used in Sections 5–7)1. *Uniform normal pressure distribution*

$$F_z = 4000 \text{ N}, v = 60 \text{ km/h}, L\sigma_{0x} = 314 \cdot 10^3 \text{ N}, \\ L\sigma_{0y} = 159.2 \cdot 10^3 \text{ N}, F_C/F_z = 0.64, F_S/F_z = 1.76, \\ v_s = 3.48 \text{ m/s}, \delta = 0.6, \sigma_1 = \sigma_2 = 0.$$

2. *Asymmetric trapezoidal normal pressure distribution*

$$F_z = 4000 \text{ N}, v = 60 \text{ km/h}, L\sigma_{0x} = 314 \cdot 10^3 \text{ N}, \\ L\sigma_{0y} = 159.2 \cdot 10^3 \text{ N}, F_C/F_z = 0.648, F_S/F_z = 1.671, \\ v_s = 3.49 \text{ m/s}, \delta = 0.6, \sigma_1 = \sigma_2 = 0, L = 0.303 \text{ m}, r_l = 0.134, r_r = 0.707.$$

B. Model Parameters as Functions of Normal Force1. *2D model*

$$\sigma_{0x} = 3.117 \cdot 10^5 F_z \\ \sigma_{0y} = (-0.168F_z^2 + 1.714F_z + 1.908) \cdot 10^5 \\ \mu_C = -0.0215F_z + 0.733 \\ \mu_S = -0.065F_z + 2.087 \\ L = 0.137 + 0.056\sqrt{F_z} \\ G_y = 0.0064F_z^2 - 0.0159F_z + 0.9641 \\ v_s = 3.15 \\ \delta = 0.6 \\ \sigma_2 = 0$$

2. *3D model*

$$\sigma_{0x} = 3.16 \cdot 10^5 F_z \\ \sigma_{0y} = (-0.18F_z^2 + 1.88F_z + 1.84) \cdot 10^5 \\ \mu_C = -0.022F_z + 0.734 \\ \mu_S = -0.054F_z + 1.887 \\ L = 0.137 + 0.056\sqrt{F_z} \\ G_y = 0.007F_z^2 - 0.028F_z + 0.98 \\ v_s = 3.5 \\ \delta = 0.6 \\ \sigma_2 = 0 \\ \phi = 0.032F_z^2 + 0.019F_z + 0.575 \\ r_l = 0.15 \\ B = 13.105, C = -9.276, D = 0.0434, E = 0.923 \\ S_v = -0.0125F_z + 0.756$$